Geochemistry, Geophysics, Geosystems®

AGU ADVANCING EARTH AND SPACE SCIENCE

RESEARCH ARTICLE
10.1029/2021GC010290

2-D Analytical P-to-S and S-to-P Scattered Wave Finite Frequency Kernels

Nicholas Harmon[1], Catherine A. Rychert[1], Yujiang Xie[1], and Petros Bogiatzis[1]

[1]Ocean and Earth Science, University of Southampton, Southampton, UK

Key Points:

- We present 2-D analytical P-to-S and S-to-P finite frequency sensitivity kernels that are rapidly calculated with low computational cost
- We demonstrate the validity of the kernels in comparison to kernels calculated using SPECFEM2D
- Analytical P-to-S kernels recover discontinuities with sharp or curved topography, and S-to-P kernels may be useful in certain situations

Supporting Information:

Supporting Information may be found in the online version of this article.

Correspondence to:

C. A. Rychert,
c.rychert@soton.ac.uk

Citation:

Harmon, N., Rychert, C. A., Xie, Y., & Bogiatzis, P. (2022). 2-D analytical P-to-S and S-to-P scattered wave finite frequency kernels. *Geochemistry, Geophysics, Geosystems*, *23*, e2021GC010290. https://doi.org/10.1029/2021GC010290

Received 3 DEC 2021
Accepted 25 MAR 2022

Author Contributions:

Conceptualization: Nicholas Harmon, Catherine A. Rychert
Formal analysis: Nicholas Harmon, Catherine A. Rychert, Yujiang Xie, Petros Bogiatzis
Funding acquisition: Nicholas Harmon, Catherine A. Rychert
Investigation: Nicholas Harmon, Catherine A. Rychert, Yujiang Xie, Petros Bogiatzis
Methodology: Nicholas Harmon, Catherine A. Rychert
Project Administration: Nicholas Harmon, Catherine A. Rychert
Resources: Nicholas Harmon, Catherine A. Rychert
Software: Nicholas Harmon

Abstract Scattered wave imaging provides a powerful tool for understanding Earth's structure. The development of finite frequency kernels for scattered waves has the potential for improving the resolution of both the structure and magnitude of discontinuities in S-wave velocity. Here we present a 2-D analytical expression for teleseismic P-to-S and S-to-P scattered wave finite-frequency kernels for a homogeneous medium. We verify the accuracy of the kernels by comparing to a spectral element method kernel calculated using SPECFEM2D. Finally, we demonstrate the ability of the kernels to recover seismic velocity discontinuities with a variety of shapes including a flat discontinuity, a discontinuity with a sharp step, a discontinuity with a smooth bump, and an undulating discontinuity. We compare the recovery using the kernel approach to expected recovery assuming the classical common conversion point (CCP) stacking approach. We find that the P-to-S kernel increases recovery of all discontinuity structures in comparison to CCP stacking especially for the shallowest discontinuity in the model. The S-to-P kernel is less successful but can be useful for recovering the curvature of shallow discontinuity undulations. Finally, although we observe some variability in the amplitude of the kernels along the discontinuities, the kernels show some potential for recovering the magnitude of the velocity contrast across a discontinuity.

Plain Language Summary Seismic waves convert from compressional waves to shear waves and vice versa at sharp discontinuities in seismic velocity. These conversions are useful for tightly constraining the structure and properties of the seismic velocity discontinuities, and this can be used to better determine the physical and chemical properties of the Earth. Typical approaches that use the converted phases to constrain discontinuities assume that the discontinuities are relatively flat, and migrate the converted phase energy to depth, stacking the converted phase energy on a grid. However, discontinuities may have significant topography, for instance in subduction zones or beneath hotspots, rifts, or ridges. There are several different approaches to account for such topography with varying degrees of success and also computational cost. One approach is to use the theoretical sensitivity kernels to distribute the converted phase energy in space. Here we present analytical sensitivity kernels for converted phases and assess their ability to recover strong discontinuity topography. The approach is very fast and computationally efficient. The compressional to shear kernel successfully retrieves all shallow discontinuity structures, while the shear to compressional kernel may be useful for constraining discontinuity curvature in certain circumstances.

1. Introduction

Scattered waves are useful for constraining Earth's discontinuities from the crust to the lower mantle. Receiver functions calculated from teleseismic P-to-S and/or S-to-P conversions are particularly successful in imaging the Moho and crustal anisotropic layers (Chichester et al., 2018; Ligorria & Ammon, 1999; Owens & Zandt, 1985; Park & Levin, 2000; Schulte-Pelkum et al., 2005), upper mantle structure such as the lithosphere-asthenosphere boundary, the mid-lithospheric discontinuity and discontinuities related to anisotropic lithospheric layering (Audet, 2016; Ford et al., 2010; Lekic et al., 2011; Levander et al., 2006; Li et al., 2004; Possee et al., 2021; Rychert & Shearer, 2009; Rychert et al., 2005), as well as the mantle transition zone discontinuities (Agius et al., 2017, 2021; Lawrence & Shearer, 2006; Shen et al., 1998; Tauzin et al., 2008). For imaging discontinuities, the simplest and most common approach is to use common conversion point (CCP) stacking, that is, migration of receiver funtions to depth through an assumed velocity model before stacking (Angus et al., 2009; Dueker & Sheehan, 1997; Rychert et al., 2012). The method assumes a 1-D layered velocity structures with little topography, where Snell's law and ray theory are valid. However, in some regions, strong topography and dip angles are expected. For instance, strong undulations in Moho depths can occur beneath subduction zone arcs, hotspots, and rifts (Hammond et al., 2011; Lavayssiere et al., 2018; Rychert et al., 2018; Schlaphorst et al., 2021). The raypaths

Supervision: Nicholas Harmon, Catherine A. Rychert
Validation: Nicholas Harmon, Catherine A. Rychert, Yujiang Xie
Visualization: Nicholas Harmon, Catherine A. Rychert, Yujiang Xie
Writing – original draft: Nicholas Harmon, Catherine A. Rychert
Writing – review & editing: Nicholas Harmon, Catherine A. Rychert, Yujiang Xie, Petros Bogiatzis

of the conversions from strongly dipping topography may be quite different from those assumed by CCP stacking (Lekic & Fischer, 2017). Therefore, tight constraints on discontinuities with strong topography have proven challenging. Better approximations to elastic wave physics are required.

Several approaches have been developed to account for heterogenous velocities in receiver function imaging to better illuminate more complex structures. Post-stack one-way wave equation migration includes 3-D filtering to account for lateral heterogeneities (Chen et al., 2005). Pre-stack depth migration involves stacking waveforms onto surfaces of constant delay time (Cheng et al., 2016; Levander, 2003; Millet et al., 2019; Poppeliers & Pavlis, 2003a, 2003b; Sheehan et al., 2000; Wilson et al., 2003). The generalised radon transform (GRT) approach uses this approach for the forward problem and inverts for scattering potential relative to a 1-D background model (Bostock et al., 2001; Liu & Levander, 2013; Rondenay et al., 2001; Shragge et al., 2001).

Full-waveform modeling and inversion can be used to invert for complex and/or heterogeneous structures, although it is more computationally expensive. Various simplifications for solving for wave propagation have been proposed to reduce the computational costs, for instance by using analytical solutions or reducing the simulation domains (Leng et al., 2016, 2019; Monteiller et al., 2013, 2015; Nissen-Meyer et al., 2014; Tong, Chen et al., 2014, Tong, Komatitsch et al., 2014). These approaches are becoming more common but are still computationally intensive compared to the other methods discussed here for the S-to-P or P-to-S kernel calculations. Central to full-waveform and ray theoretical inversion schemes are the sensitivity kernels that relate the scattered phases or receiver functions to the theoretical predictions for the spatial sensitivity to changes in Earth structure. These kernels are implicit in the constructions discussed above.

Recent work has explicitly presented the finite frequency kernels for scattered waves using the kernel formulated in the work of Bostock et al. (2001) and Dahlen et al. (2000), including work by Mancinelli and Fischer (2018), Hansen and Schmandt (2017) and Bogiatzis et al. (2022). The kernels were calculated via ray tracing through a layered model (Mancinelli & Fischer, 2018), using the fast marching method and assuming geometrical spreading for a homogeneous medium (Hansen & Schmandt, 2017; Hua et al., 2020), and using the shortest path method and Dijkstra's algorithm and accounting for geometrical spreading in heterogeneous media (Bogiatzis et al., 2022). The fast marching and shortest path methods provide a means for efficient raytracing which is required to calculate kernels based in ray theory. The fast marching method is a means of rapidly solving eikonal equation problems by monotonically advancing fronts to obtain traveltime fields (Sethian, 1996). The shortest path method uses Dijkstra's algorithm (Dijkstra, 1959) to calculate the traveltime fields between points in a graph or network (Bogiatzis et al., 2021).

Recent work has revealed several advantages and limitations of using finite frequency kernels for scattered wave conversions. The kernels were applied to synthetic full-waveform receiver functions to illustrate the recovery of structures such as undulating discontinuities (Bogiatzis et al., 2022; Mancinelli & Fischer, 2018), sharply dipping discontinuities (Hua et al., 2020), and subduction zone structures (Hansen & Schmandt, 2017). The work of Mancinelli and Fischer (2018) showed that discontinuities with 100–200 km wavelength and topography of ±10–20 km can be recovered for secondary discontinuities, for example, discontinuities beneath the Moho, by S-to-P kernels if the kernel are calculated through a layered structure that resembles the real structure. However, S-to-P was not able to recover larger topography or higher frequency undulations. The study of Hansen and Schmandt (2017) demonstrated the ability of the P-to-S kernels to recover dipping vertical subduction zone topography, with S-to-P being less successful. The work of Hua et al. (2020) demonstrated that the S-to-P kernel can be used to image discontinuities with dips of <20° and also dips of 40–50° with careful weighting and an optimal station geometry. The study of Bogiatzis et al. (2022) demonstrated that P-to-S and S-to-P kernels can recover Gaussian topography with an amplitude of 20 km with minimal artifacts, the P-to-S kernel recovers sinusoidal topography with an amplitude of ±20 km and a wavelength of 200 km well, and the S-to-P kernel can recover the curvature of the sinusoid. The work of Bogiatzis et al. (2022) also demonstrated that accounting for heterogeneous structure can lead to up to a 30% improvement in waveform amplitudes in comparison to the assumption of geometric spreading for a homogeneous Earth in a subduction zone setting. The approaches of Hansen and Schmandt (2017) and Mancinelli and Fischer (2018) focused in particular on the imaging problem rather than the recovery of the magnitudes of the velocity discontinuities, and all four studies required moderate amounts of computational cost. In addition, scattered wave finite frequency kernels have been applied to discontinuities as deep as the mantle transition zone (Zhang & Schmandt, 2019; Zhou, 2018).

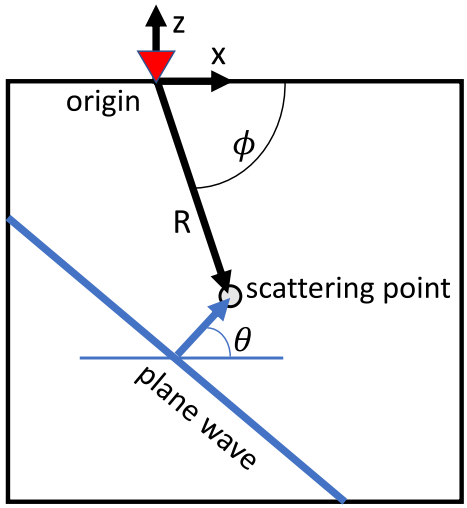

Figure 1. Coordinate schematic. The cartesian *x*- and *z*-axes are indicated, with the station located on the origin (red triangle). The distance and angle between the origin and the scattering point are described by the cylindrical coordinates R and ϕ, respectively. The incident plane wave (blue) and associated angle measured from horizontal (θ) are shown.

Here we present a closed form of the 2-D analytical P-to-S and S-to-P scattered wave finite frequency kernels. These kernels assume a homogeneous Earth, and therefore do not include the effects of structural heterogeneity like the previously described approaches. Although the kernels could easily be extended to 3-D, we investigate the 2-D case here, as a first step and for the sake of simplicity and also given that many tectonic environments, for instance rifts (e.g., Armitage et al., 2015; Chambers et al., 2021, 2019; Lavayssiere et al., 2018; Rychert et al., 2012), ridges (e.g., Harmon et al., 2020, Harmon, Wang et al., 2021, 2018; Agius et al., 2021, 2018; Eakin et al., 2018; Rychert et al., 2021, 2018; Rychert et al., 2020; Saikia et al., 2021b, 2021a; Wang et al., 2020), or subduction zone trenches (e.g., Harmon et al., 2013, Harmon, Rychert et al., 2021, 2008; Chichester et al., 2020; Cooper et al., 2020; Harmon & Rychert, 2015; Rychert et al., 2008; Schlaphorst et al., 2021; Syracuse et al., 2008) are often characterized by at least some structures that are expected to be relatively 2-D. The idea is to determine the utility of using the simplest and computationally efficient way to implement a kernel and also recover the magnitude of velocity discontinuities. We verify the kernels against kernels calculated using SPECFEM2D (Komatitsch et al., 2012; Tromp et al., 2008). We evaluate the ability of these analytical kernels to recover a variety of discontinuity structures in comparison to classical CCP approaches.

2. Methods

2.1. 2-D Analytical Solutions for P-to-S and S-to-P Scattered Waves for a Homogeneous Medium

We begin with the Fourier transform of the wave equation and assume an isotropic homogeneous medium:

$$-\rho\omega^2\mathbf{u}(\omega) = \left(\kappa + \frac{4}{3}\mu\right)\nabla^2\mathbf{u}(\omega) - \mu\nabla\times\nabla\times\mathbf{u}(\omega) + \mathbf{f}(\omega) \tag{1}$$

where ρ is density, ω is angular frequency, $\mathbf{u}$ (u, v) is the displacement vector, κ and μ are the bulk and shear elastic moduli, respectively, and $\mathbf{f}$ is the body force of the initial source. We use a polar coordinate system $\mathbf{X}$ (R, ϕ), where R is radius and ϕ is the angle from the x-axis in a Cartesian coordinate system (Figure 1). The receiver is located at $R = 0$. Finite frequency kernels can be constructed from a forward solution for a presumed incoming plane wavefield $\mathbf{u}$ and a scattered adjoint wavefield $\mathbf{u}^\dagger$ that consists of the simultaneous, time-reversed signal from the receiver, that is, as if the receiver were a simultaneous, fictitious source (Liu & Tromp, 2006; Tromp et al., 2005). Based on first-order perturbation theory the single frequency sensitivity kernels for λ and μ can be expressed as:

$$\mathrm{K}_\mu(\omega,\mathbf{X}) = 2\mu\boldsymbol{D}^\dagger : \boldsymbol{D} \tag{2}$$

$$\mathrm{K}_\kappa(\omega,\mathbf{X}) = \kappa\left(\nabla\cdot\boldsymbol{u}^\dagger\right)(\nabla\cdot\boldsymbol{u}) \tag{3}$$

where $\mathbf{D}$ and $\mathbf{D}^\dagger$ denote the strain deviator and its adjoint, respectively.

And in terms of S-wave speed ($\mathrm{V_s}$) and P-wave speed ($\mathrm{V_p}$):

$$\mathrm{K}_{\mathrm{V_s}}(\omega,\mathbf{X}) = 2\left[\mathrm{K}_\mu(\omega,\mathbf{X}) - \frac{4\mu}{3\kappa}\mathrm{K}_\kappa(\omega,\mathbf{X})\right] \tag{4}$$

$$\mathrm{K}_{\mathrm{V_p}}(\omega,\mathbf{X}) = 2\left(\frac{\kappa+\frac{4}{3}\mu}{\kappa}\right)\mathrm{K}_\kappa(\omega,\mathbf{X})$$

where K_κ is zero because the divergence of a S-wave field is zero (Equation 3). This means that $\mathrm{K}_{\mathrm{V_p}}$ is also zero. This is true for S-to-P imaging because the source is an S-wave, and it is true for P-to-S because the adjoint is

an S-wave. It is also consistent with previous work that reported no V_p dependence for scattered wave imaging (Bank & Bostock, 2003; Rychert et al., 2007). For the wavefields for the scattered wave system, we assume an incoming shear plane wave of amplitude A, in the 2-D plane and a forward scattering to the receiver at $R = 0$. For P-to-S, the incoming 2-D plane wave displacement at any point in $\mathbf{X}$ at a given P-wave slowness ($\frac{\sin(\phi-\theta)}{V_p}$) at a given angle θ, corresponding to the angle of the incident plane wave from horizontal (taken from the positive x direction) is given by:

$$\begin{bmatrix} u(\omega,\mathbf{X}) \\ v(\omega,\mathbf{X}) \end{bmatrix} = A(\omega)\exp\left(-\frac{i\omega R\sin(\phi-\theta)}{V_p}\right)\begin{bmatrix} \cos(\theta) \\ \sin(\theta) \end{bmatrix} \tag{5}$$

The adjoint or incoming scattered S-wavefield due to an applied unit adjoint force in the θ direction to the receiver can be described in 2-D as:

$$\begin{bmatrix} u^{\dagger}(\omega,\mathbf{X}) \\ v^{\dagger}(\omega,\mathbf{X}) \end{bmatrix} = A^{\dagger}(\omega)\frac{1i}{4\rho V_S}\begin{bmatrix} H_0^{(1)}\left(\frac{\omega R}{V_S}\right)\frac{\cos(2\phi-\theta)-\cos(\theta)}{2V_S} - H_2^{(1)}\left(\frac{\omega R}{V_S}\right)\frac{\cos(2\phi-\theta)}{R\omega} \\ H_0^{(1)}\left(\frac{\omega R}{V_S}\right)\frac{\sin(2\phi-\theta)-\sin(\theta)}{2V_S} - H_2^{(1)}\left(\frac{\omega R}{V_S}\right)\frac{\sin(2\phi-\theta)}{R\omega} \end{bmatrix} \tag{6}$$

where $H_{0,2}{}^{(1)}$ are Hankel functions of the first kind of 0th and 2nd order and are Green's functions for P- and S-waves in 2-D and $A^{\dagger}$ is the adjoint source amplitude (Sanchezsesma & Campillo, 1991). Substituting Equations 5 and 6 into Equations 2–4, we get:

$$K_{V_S}(\omega,\mathbf{X}) = A(\omega)A^{\dagger}(\omega)\exp\left(\frac{-i\omega R\cos(\phi-\theta)}{V_P}\right)\left[H_1^{(1)}\left(\frac{\omega R}{V_s}\right)\left(\frac{\omega^2(\sin(3\phi-3\theta)+\sin(\phi-\theta))}{4V_PV_S} - \frac{2V_S\sin(3\phi-3\theta)}{V_PR^2}\right) + H_0^{(1)}\left(\frac{\omega R}{V_s}\right)\frac{\omega\sin(3\phi-3\theta)}{V_PR}\right] \tag{7}$$

$H_1{}^{(1)}$ is the Hankel function of the first kind of 1st order. The unit of this kernel (Equation 7) is [m^{-2}]. To produce the kernel for a traveltime misfit kernel we multiply the sum of kernels over all frequencies by the time series length of the adjoint source, T:

$$K_{V_S}(t,\mathbf{X}) = T\sum_{i=2}^{\frac{N}{2}} K_{V_S}(\omega_i,\boldsymbol{X}) \tag{8}$$

For the S-to-P case the incoming plane wavefield is described by a S-wave horizontal slowness of ($\frac{\sin(\phi-\theta)}{V_s}$):

$$\begin{bmatrix} u(\omega,\mathbf{X}) \\ v(\omega,\mathbf{X}) \end{bmatrix} = A(\omega)\exp\left(-\frac{i\omega R\sin(\phi-\theta)}{V_s}\right)\begin{bmatrix} \sin(\theta) \\ -\cos(\theta) \end{bmatrix} \tag{9}$$

And the adjoint field is given by:

$$\begin{bmatrix} u^{\dagger}(\omega,\mathbf{X}) \\ v^{\dagger}(\omega,\mathbf{X}) \end{bmatrix} = A^{\dagger}(\omega)\frac{1}{8i\rho V_P^2}\begin{bmatrix} \left(H_0^{(1)}\left(\frac{\omega R}{V_P}\right)\right)\cos\theta - \cos(2\phi-\theta)H_2^{(1)}\left(\frac{\omega R}{V_P}\right) \\ \left(H_0^{(1)}\left(\frac{\omega R}{V_P}\right)\right)\sin\theta - \sin(2\phi-\theta)H_2^{(1)}\left(\frac{\omega R}{V_P}\right) \end{bmatrix} \tag{10}$$

(Sanchezsesma & Campillo, 1991). Applying Equations (2) and (4) to (9) and (10) gives the S-wave velocity kernel for S-to-P:

$$K_{V_S}(\omega,X) = A(\omega)A^{\dagger}(\omega)\exp\left(\frac{-i\omega R\cos(\phi-\theta)}{V_p}\right)\left[H_1^{(1)}\left(\frac{\omega R}{V_s}\right)\left(\frac{\omega^2(\sin(3\phi-3\theta)+\sin(\phi-\theta))}{4V_pV_s} - \frac{2V_S\sin(3\phi-3\theta)}{V_PR^2}\right) + H_0^{(1)}\left(\frac{\omega R}{V_s}\right)\frac{\omega\sin(3\phi-3\theta)}{V_PR}\right] \tag{11}$$

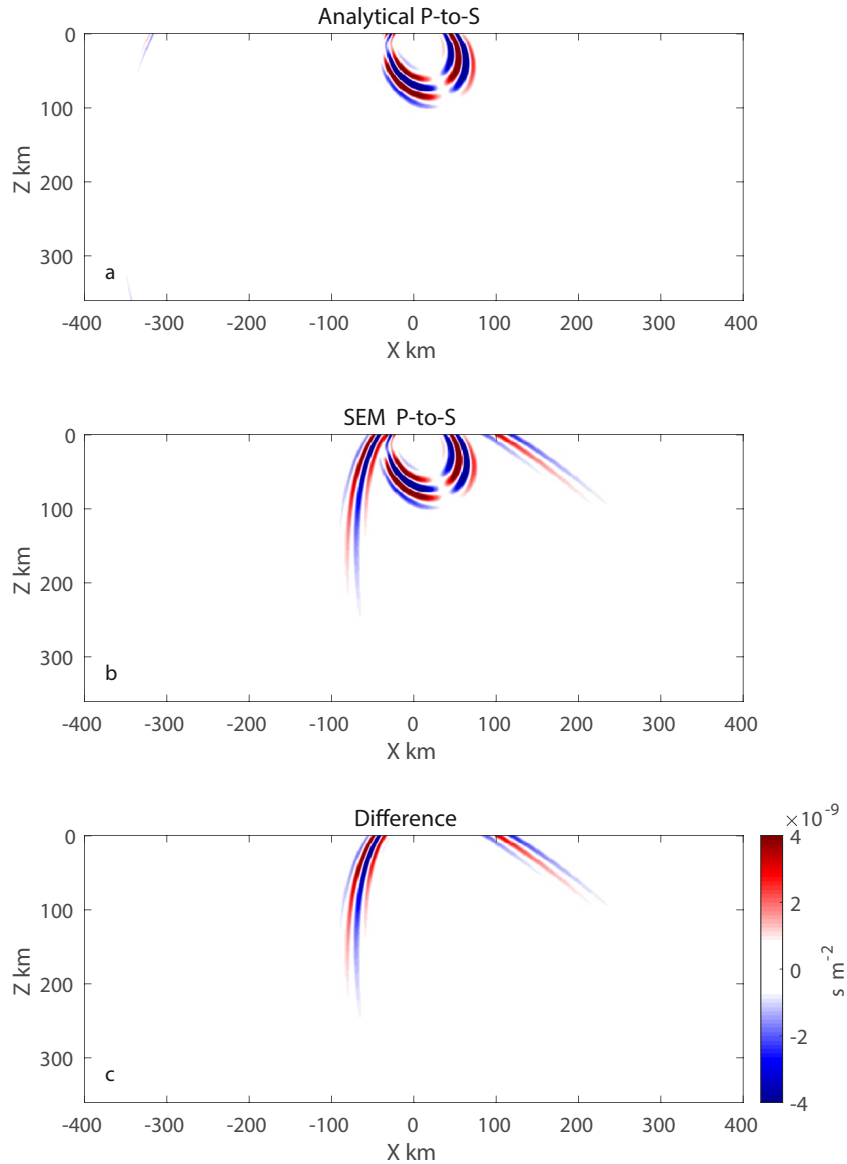

Figure 2. The P-to-S kernel (K_{V_s}) calculated analytically in comparison to the P-to-S kernel calculated using SPECFEM2D. The kernels are for a homogeneous medium. We present: (a) the analytical kernel, (b) the SEM kernel, and (c) the difference between the analytical and SEM kernels.

2.2. Models, Source, Adjoint Source, and Mesher

The analytical kernel solution is for a homogeneous background model. The material properties of the homogenous model are: ρ = 2,500 kg m^{-3}, V_p = 6.12 km s^{-1}, and V_s = 3.5 km s^{-1}. The analytical kernel is calculated on a 1 km by 1 km grid.

To verify the analytical kernels we use the SPECFEM2D package to calculate Fréchet kernels, the first-order derivatives of the seismic misfit functional with respect to the model parameters, which are expressed in wave speed and density (Tromp et al., 2005). The full-waveform misfit P-to-S kernel for a two-layer model is shown in the work of Tong, Chen, et al. (2014). We show the full-waveform S-to-P kernel for a two-layer model calculated using SPECFEM2D for comparison (Figure S1). The full-waveform kernel has sensitivity to both V_p and V_s and is comprised of both an S-to-P scattered wave kernel component, such as that presented here (Figures 2–5), and also "banana-doughnut" shaped kernel components, such as those used for direct P- and S- waves. The additional

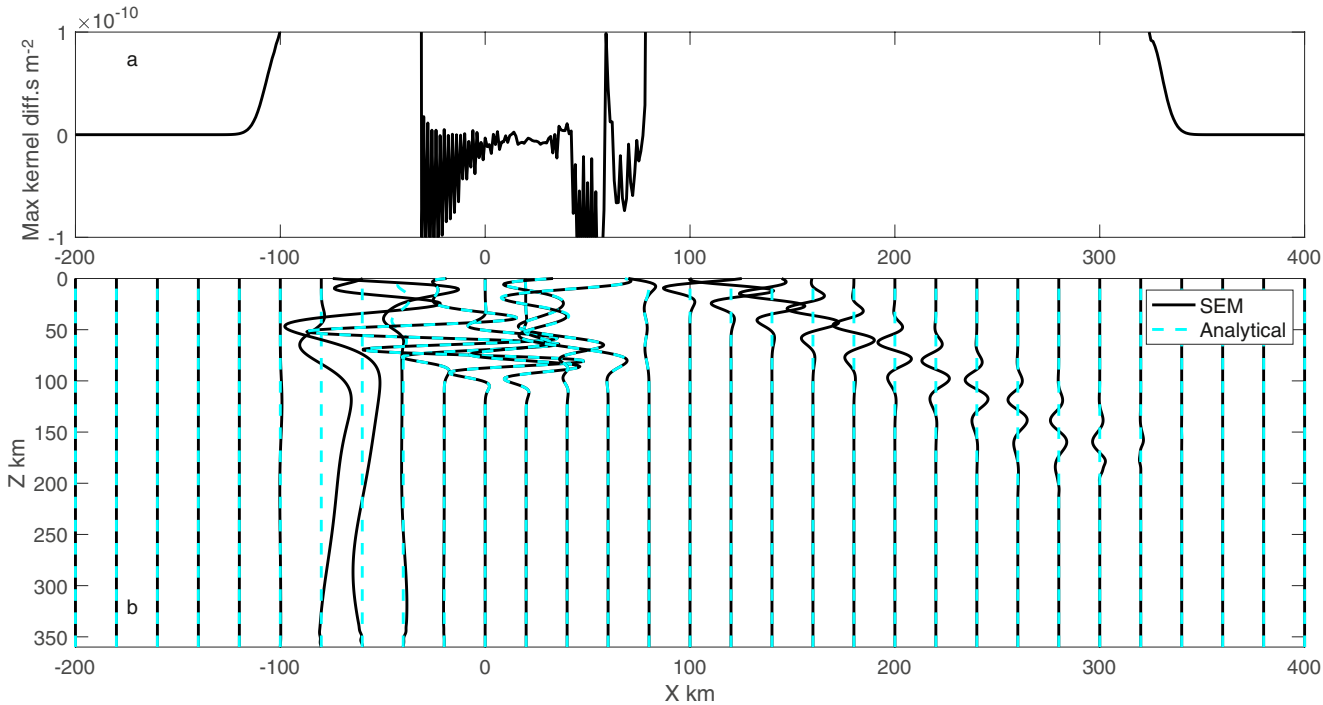

Figure 3. The difference between the analytical and the SEM P-to-S kernels (K_{V_s}). We show (a) the maximum difference between the two kernels at every horizontal position and (b) individual cross sections through the kernel. The analytical kernel cross sections are in dashed cyan, and the SEM cross-sections are in black. The largest difference is caused by the fact that the SEM simulation also includes an artificial adjoint P-wave component, which also interacts with the incoming P-wave. This component is not included in the analytical kernel. The remaining small oscillatory differences are caused by the interpolation of the SEM kernel onto a regular grid.

sensitivity, in comparison to the kernels used here, arises from the interaction of the forward scattered P-wave and the adjoint P-wave source, which gives sensitivity of the waveform to V_p heterogeneities in the upper layer; a similar component sensitivity is visible in the lower layer in the V_s kernel where the forward propagating S-wave interacts with the scattered S-wave from the adjoint P-wave source at the interface.

Without a velocity discontinuity, SEM calculations do not produce a scattered phase that can be used as the adjoint source for the kernel calculation. The adjoint source and full-waveform kernel for a homogeneous medium are zero. The full-waveform kernel for the case of an actual two-layer model includes additional sensitivity in comparison to our kernel as discussed in the previous paragraph (Figure S1). Therefore, a different approach is needed to construct the kernel for a hypothetical discontinuity relative to a homogeneous background model, that is, the scenario under which our analytical kernels are constructed for scattered waves. The kernel for a hypothetical discontinuity can be constructed by running SPECFEM2D simulations for adjoint sources at many points throughout the model domain to populate the kernel for a given time delay and incidence angle, that is, essentially assuming that every point in the model is a scatterer (Mancinelli & Fischer, 2018). We use an alternative approach. We implement a Ricker wavelet with the dominant frequency of 0.25 Hz rotated perpendicular to the P-wave arrival angle as the adjoint source for P-to-S in SPECFEM2D. We do the same for the S-to-P adjoint source but rotating into the S-wave arrival angle. The interaction between the adjoint and the incident plane wave, also a Ricker wavelet with a dominant frequency of 0.25 Hz, in the SEM simulation gives a scattered wave kernel for a theoretical discontinuity at a given offset that is suitable for benchmarking and comparison purposes. This approach involves one forward and one adjoint simulation for each kernel, and therefore is a relatively efficient way of verifying our analytical kernels. The amplitudes of the source and adjoint source wavelets are the same and normalized by the sum of the spectral amplitude at all frequencies. This allows for simple and direct comparison with the SEM kernels. This results in a scattered wave traveltime misfit kernel equivalent to our analytical kernels shown in Figures 2–5. The amplitude of the adjoint source $A^{\dagger}(\omega)$ and source $A(\omega)$ are normalized and dimensionless, so the resulting kernel in Equation 8 is a traveltime kernel and has units [s m^{-2}]. The adjoint source in Equations 6 and 10 for the traveltime kernel has units of [s^2 m kg^{-1}]. Source and adjoint amplitudes are

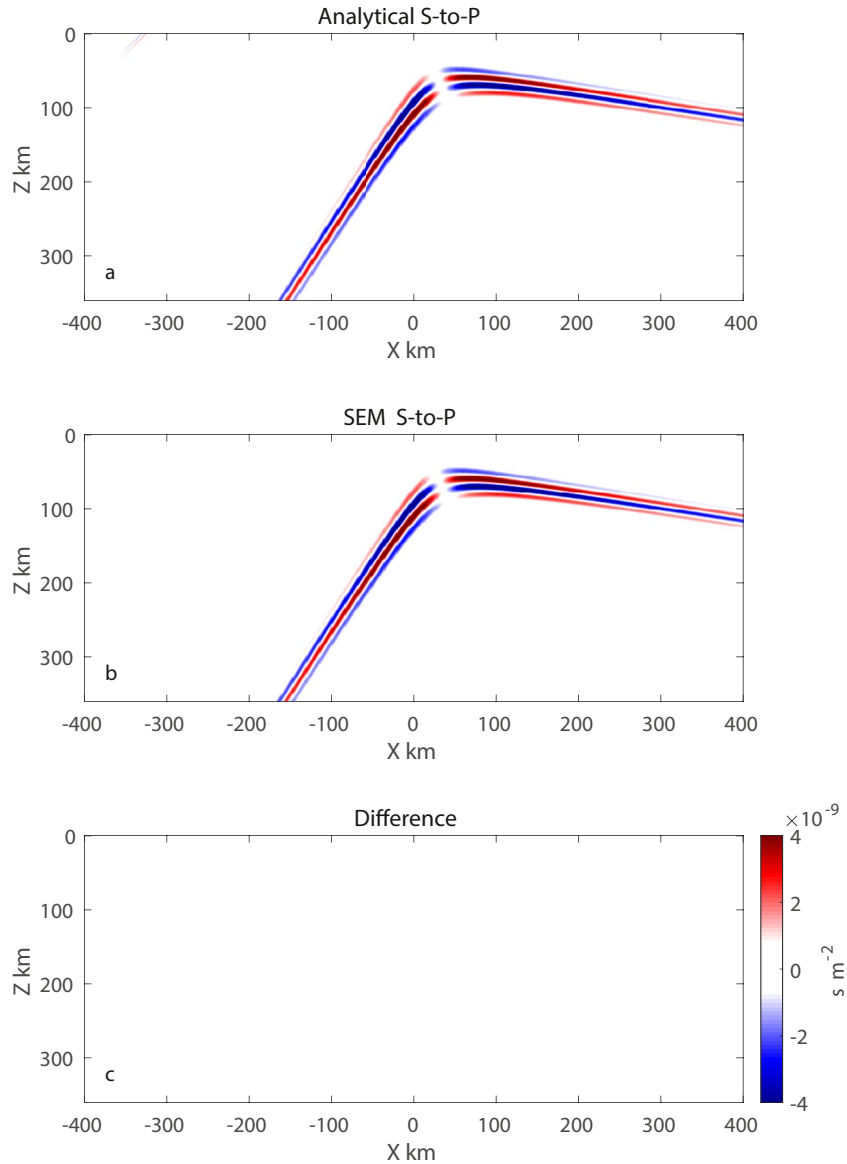

Figure 4. The S-to-P kernel (K_{V_s}) calculated analytically in comparison to the S-to-P kernel calculated using SPECFEM2D. The kernels are for a homogeneous medium. We present: (a) the analytical kernel, (b) the SEM kernel, and (c) the difference between the analytical and SEM kernels.

not normalised in the kernels used in the recovery tests, which is required to recover the magnitude of velocity discontinuities, and this results in different units, which we will discuss in greater detail in subsequent sections.

We examine the ability of the 2-D analytical kernels to recover Earth structure. To create synthetic seismogram predictions we run SPECFEM2D simulations through a two-layer model with a variety of discontinuity topographies. The two-layer models assume the properties of the homogeneous model for the shallow layer and the following properties for the deeper layer: $\rho = 3{,}300$ kg m^{-3}, $V_p = 8.1$ km s^{-1}, and $V_s = 4.5$ km s^{-1}, in other words, causing a discontinuity associated with a 28% velocity increase with depth. We examine the ability of the analytical kernels to resolve four different boundary topographies: a flat layer at 100 km depth, a sinusoidal topography with a wavelength of 200 km and amplitude of $\pm$20 km centered at a depth of 100 km, a discontinuity at 50 km with a 20 km step down step over 20 km distance, and a discontinuity at 100 km depth with a 20 km high bump characterized by a Gaussian with $\sigma = 35$ km. The previously described discontinuities avoid potential artifacts from free-surface multiples that arrive after the direct P-to-S conversion, since the multiples arrive much later.

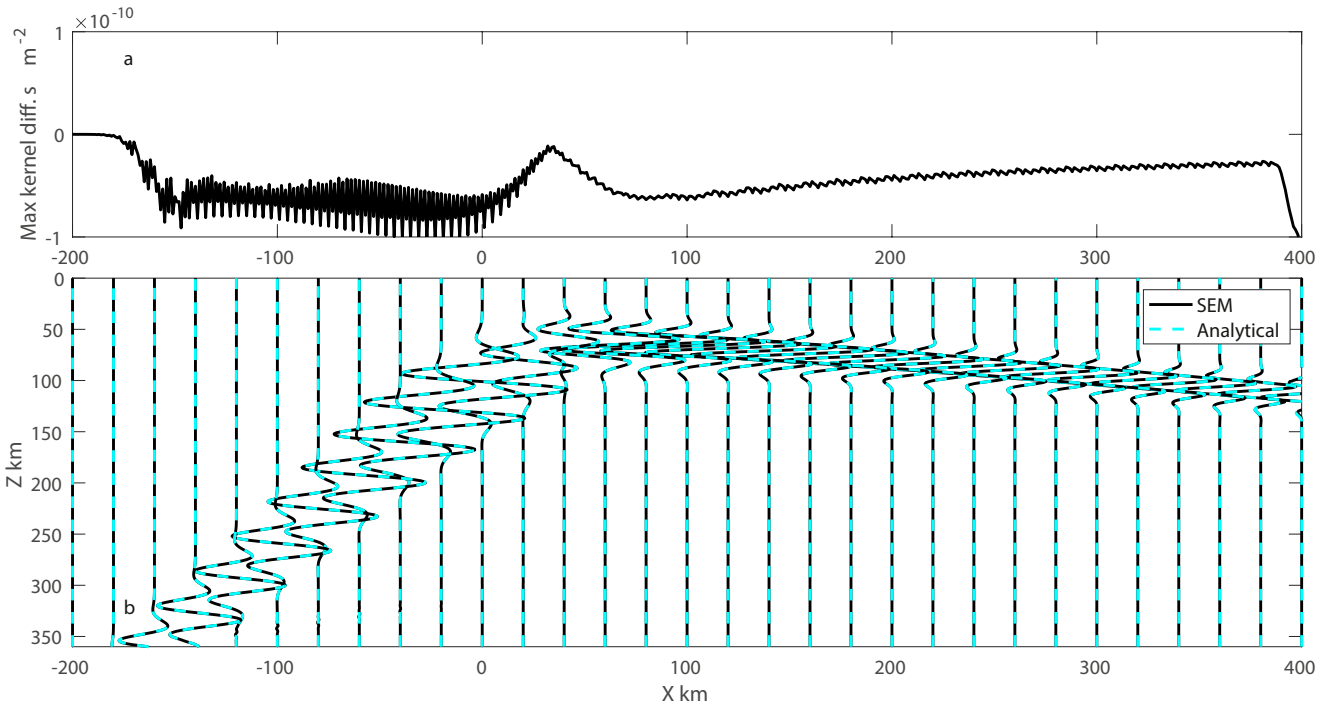

Figure 5. The difference between the analytical and the SEM S-to-P kernels (K_{V_s}). We show (a) the maximum difference between the two kernels at every horizontal position and (b) individual cross sections through the kernel. The analytical kernel cross sections are in dashed cyan, and the SEM cross-sections are in black.

However, we also test the Gaussian bump with $\sigma = 35$ km and amplitude of 15 km in depth and the sinusoid with a wavelength of 200 km and amplitude of ±20 km at a depth of 30 km to evaluate recovery at realistic Moho depths. The tests also allow us to evaluate variability in recovery with depth and also potential artifacts from the multiples. Finally, we test a model with a flat Moho at 30 km depth and a deeper drop in velocity, a lithosphere-asthenosphere boundary phase at 80 km depth with a step down of 20 km over 20 km distance. The Moho velocity contrast is the same as that of the single discontinuity tests and the layer beneath the lithosphere-asthenosphere boundary has a $V_p = 7.92$ km s^{-1}, $V_s = 4.05$ km s^{-1}, and $\rho = 3{,}300$ kg m^{-3}, in other words, creating a discontinuity characterized by a 10% velocity decrease with depth. This final test is to evaluate the recovery of features deeper than the shallowest discontinuity.

To calculate synthetic data through these models we use the internal mesher of the SPECFEM2D package. For P-to-S we use plane waves with incidence angles of 29° and 32°. For S-to-P we use plane waves with incidence angles of 23° and 26°. These angles are within the typical range used in receiver function studies, which vary from approximately 23°–40° for P-to-S and 25°–33° for S-to-P. Including additional angles would improve recovery. Due to symmetry we are able to illuminate the structures using the two simulations by reflecting the kernels on a vertical symmetry axis. We use a 4 s dominant period Ricker source wavelet for all simulations. We place 400 spectral elements in the horizontal direction and 360 elements in the vertical direction, leading to ∼500 and ∼250 m grid spacing in the horizontal and vertical direction, respectively. We use five Gauss–Lobatto–Legendre points per element. The time interval dt for the simulation is set to 0.01 s and a total number of 10,000 time steps are used.

We use synthetic seismograms from 151 stations located from 50 to 350 km distance in the model, spaced every two km. We apply a free-surface transform to the data (Bostock, 1998). The parent phase is windowed with a 6 s Tukey window. The daughter phase has a mute applied during the 6 s of the parent phase arrival. The windowed and muted daughter component is Fourier transformed and used to calculate the kernel. We use the velocity of the shallow layer to calculate the kernels. The kernels are constructed for all combinations of sources and stations and then stacked.

We then estimate $\delta V_s/V_s$ from the synthetic seismograms by performing one step in the conjugate gradient method. We calculate the misfit or objective function, χ^2, from the daughter phase in the free-surface transformed data by summing the absolute value squared of the Fourier transformed data:

$$\chi^2 = T \sum_{j=1}^{M} \sum_{i=1}^{NFFT/2} |A_j^{\dagger}(\omega_i)|^2 \tag{12}$$

where M is the number of seismograms and NFFT/2 is the half number of frequencies in the Fourier transform. Equation 12 is a full-waveform misfit function.

The change in the misfit function due to relative changes in the material properties is given by:

$$\delta\chi^2 = \iint \left(K_{V_S} \frac{\delta V_s}{V_s} + K_{V_P} \frac{\delta V_P}{V_P} + K_\rho \frac{\delta\rho}{\rho} \right) dxdz \tag{13}$$

and we seek to minimize, χ^2 with changes to the material properties via:

$$\chi^2 + \delta\chi^2 = 0 \tag{14}$$

We ignore the V_p and ρ terms in $\delta\chi^2$. In the construction of K_{V_S} used for the recovery tests the units of the adjoint source amplitude $A^{\dagger}(\omega)$ and source amplitude, $A(\omega)$, are [m] as they are unnormalized seismograms (unlike those in Figures 2–5) and the adjoint unit (Equations 6 and 10) is [s^2 m^2 kg^{-1}]. The final K_{V_S} unit is [s]. We are only using the P-to-S and S-to-P forward scattered wave components here, that is, excluding the additional P-to-P and S-to-S components typically included in full-waveform kernels such as that shown in Figure S1.

We then assume that $\delta V_s/V_s$ is proportional to the negative of the stacked misfit kernel, $\mathbf{p} = -\mathbf{K}_{V_S}^{\text{Stacked}} dxdz$, where $\mathbf{K}_{V_S}^{\text{Stacked}}$ is the column vector of the stacked kernel, and solve for a coefficient ν (step size in the conjugate gradient) that minimizes the misfit function where $\frac{\delta V_s}{V_s} = \nu\mathbf{p}$:

$$\chi^2 - \nu\mathbf{p}^T\mathbf{p} = 0 \tag{15}$$

$$\nu = \frac{\chi^2}{\mathbf{p}^T\mathbf{p}} \tag{16}$$

Although using further iterations, instead of the one step conjugate gradient approach could potentially increase recovery, additional forward simulations would be required to update the misfit functions at greater computational cost. Therefore, our approach could be useful as an efficient first step in a more computationally intensive workflow.

For comparison purposes we also generate CCP stacks from the synthetic data. We apply a free-surface transform to the data, and the data are windowed in the same way described above. The receiver function is calculated by spectral division of the daughter component by the parent component. The data are migrated through a homogeneous velocity model with a 1 × 1 km bin size assuming the velocity of the shallow layer described above and stacked. We apply a lateral smoothing to the final image of 25 km, an approximation to Fresnel zone smoothing, similar to that used in previous work (Rychert et al., 2012). We flip the polarity of the S-to-P CCP stacks to make the images consistent with P-to-S as typically done in previous work (Rychert et al., 2012).

3. Result

3.1. Kernel Results

The analytical and SEM P-to-S scattered wave kernels for a conversion with delay time of 10 s are shown in Figure 2. The P-to-S kernels curve back toward the receiver. The P-to-S analytical kernel is similar to that from SEM. The main difference between the two is that the SEM kernel has additional linear bands extending away from the receiver location outside the central kernel structure. These are artifacts of implementing an adjoint S-wave source with a Ricker wavelet, since it cannot be done easily in an elastic SEM code without also causing a P-wave component. The artifacts are caused by the P-wave component of the adjoint source interacting with

the incident planar P-wave. Excluding the artifacts there is an excellent match in terms of the remaining portion of the kernel, with differences typically more than an order of magnitude smaller than the kernel ($<10^{-10}$ s m^{-2} vs. 4×10^{-9} s m^{-2}) (Figure 3). The small oscillatory differences are the result of interpolation of the SEM kernel onto a regular grid.

The analytical and SEM S-to-P scattered wave kernels for a conversion with delay time of 10 s are shown in Figure 4. The kernels show the distinctive "boomerang" pattern with low sensitivity near the ray theoretical conversion point, and long tails of sensitivity extending in two directions away from the receiver, one at a sub-horizontal angle and the other at a steeper angle (Hansen & Schmandt, 2017; Mancinelli & Fischer, 2018). The tails in both the SEM and analytical kernels decrease in amplitude away from the conversion point. Again there is good agreement between the analytical kernel and the SEM kernel, with differences that are an order of magnitude smaller than the kernel ($<10^{-10}$ s m^{-2} vs. 4×10^{-9} s m^{-2}) (Figure 5). As with P-to-S kernels the small differences between the analytical and SEM kernels result from the interpolation of the SEM result onto a regular grid. There are no artifacts in this case, since the adjoint S-wave is delayed relative to the incoming plane S-wave and therefore has no interaction with the adjoint.

The shapes of the kernels reflect the differential traveltime isochrons. The differences in the curvature between the P-to-S and S-to-P scattered wave kernels reflect the differences between the relative velocity of the scattered phase compared to the direct arrival.

3.2. Recovery Results

The discontinuities are recovered as phase pairs (Figures 6–9), that is, a negative phase followed by a deeper positive phase for a velocity increase with depth like the Moho or a positive phase followed by a deeper negative phase for a velocity decrease with depth like the lithosphere-asthenosphere boundary. This is the expected model perturbation for recovery of a discontinuity relative to a homogeneous background and is typical for scattered wave kernel imaging and in agreement with several other studies (Mancinelli & Fischer, 2018; Pearce et al., 2012; Rondenay et al., 2001, 2008). Some studies apply a phase shift to the receiver functions in order to recover a single phase centered on the discontinuity for ease of visualisation and interpretation (Hansen & Schmandt, 2017; Hua et al., 2020), whereas other studies report that phase shifting results in further issues with side lobes and instability (Mancinelli & Fischer, 2018). Regardless of how presented, scattered wave kernels such as those presented here recover a change in velocity, rather than the absolute velocity of the layers. For instance, a negative discontinuity, a velocity decrease with depth, could be caused by either a relatively fast shallow layer or a relatively slow deeper layer, and whether the former or the latter is the case is not recovered. The scattered wave kernels are different from full-waveform kernels which provide information about perturbations from absolute velocities (Tong, Chen, et al., 2014; Figure S1).

Both analytical P-to-S and analytical S-to-P kernels effectively recover flat discontinuities beneath the array (Figures 6a and 7a). The velocity contrasts recovered are 14%–22% for P-to-S and 12%–27% for S-to-P in comparison to the 28% input model. There are artifacts in the P-to-S kernel recovery at far distances and shallow depths. These appear in all of the P-to-S images and could be mitigated by expanding the lateral extent of the seismic array or down-weighting the outer limits of the model. For the most part the kernel recovery of flat structure is structurally just as good as that using the CCP stacking approach (Figures 6b and 7b).

Recovery of the step discontinuity is best for the case of the analytical P-to-S kernel (Figure 5c) in comparison to the analytical S-to-P kernel (Figure 7c) and the P-to-S and S-to-P CCP stacking approach (Figures 5d and 7d). The P-to-S kernel recovers the step well, including the sharp near vertical step edges. The magnitude of recovery is 20%–29% along the entire step beneath the array in comparison to the 28% input model. The kernel recovery of structure is better than the CCP stacking approach which only recovers the flat portions of the step model and includes additional artifacts, with smearing past the lateral extent in the location of the step by 10–20 km. The S-to-P kernel recovers the flat portions of the step discontinuity but not the near-vertical edges of the step. The magnitude of the recovered discontinuity is up to 34% in the deeper portions of the step and up to 15% in the shallower portions of the step in comparison to the 28% input model. In addition, the shallow and deep portions of the S-to-P kernel result are artificially smeared beyond the location of the step edge by 40–50 km. The CCP

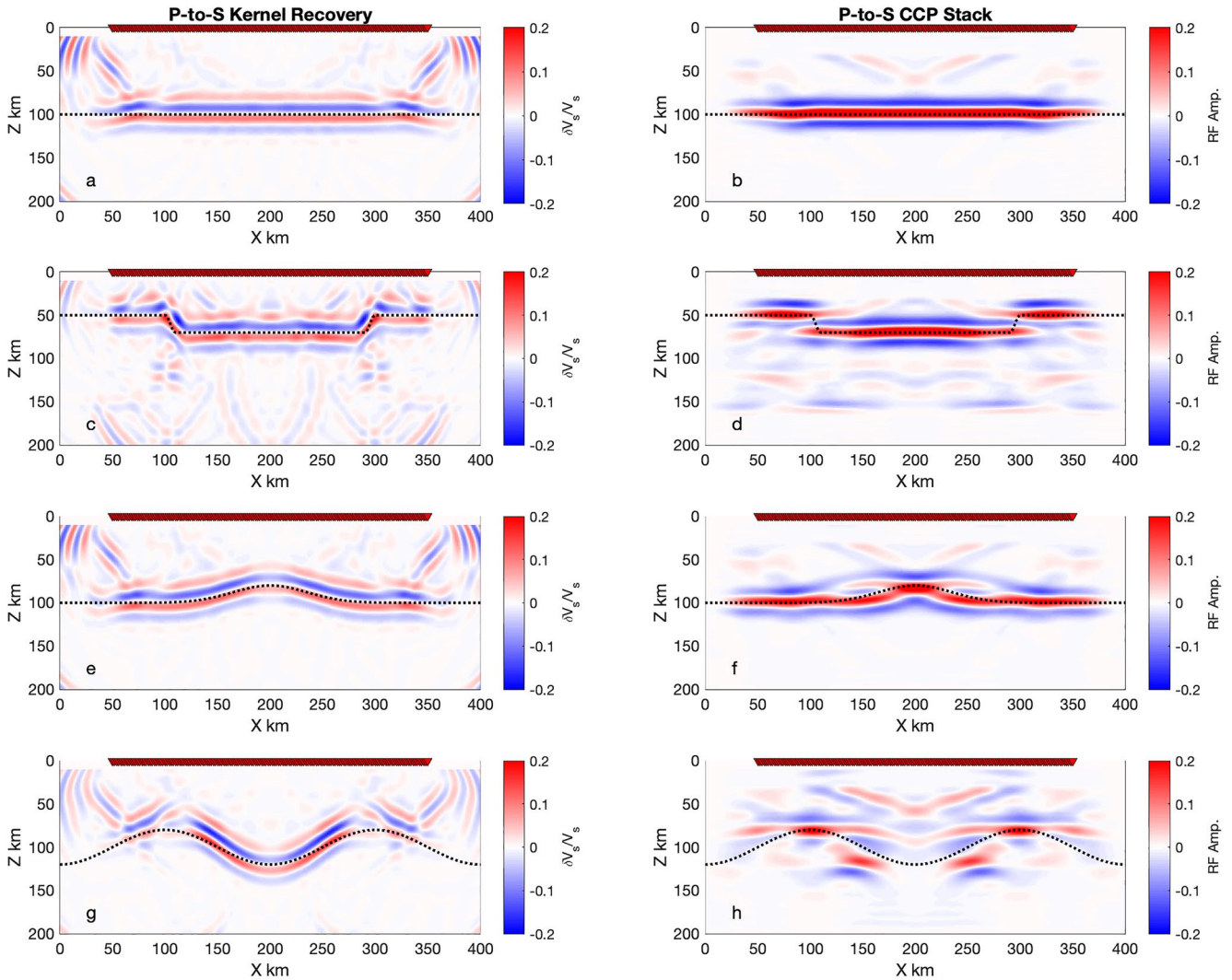

Figure 6. Recovery of velocity discontinuities at 50–120 km depth using analytical P-to-S kernels (left) in comparison to the common conversion point stacking approach (right). We present recovery of (a, b) a flat discontinuity at 100 km depth (c, d) a discontinuity with a step from 50 to 70 km depth over 20 km distance (e, f) a discontinuity at 100 km with a Gaussian bump with $\sigma = 35$ km and amplitude 20 km in depth, and (g, h) sinusoidal topography centered at 100 km depth with amplitude of ± 20 km and wavelength of 200 km.

stacking approach also recovers the flat regions of the step model, but not the more vertical steps. The S-to-P CCP stacking result is characterized by less artifacts than the analytical kernel result.

The analytical P-to-S kernel (Figure 6e) recovers the structure of the bump discontinuity at 100 km depth best in comparison to the analytical S-to-P kernel (Figure 7e) and also the P-to-S (Figure 6f) and S-to-P CCP stacking approaches (Figure 7f). The P-to-S CCP stacking approach underestimates the lateral scale of the bump. The top of the bump is also artificially smeared laterally, by 50–70 km on either side. The magnitude of the P-to-S kernel recovery ranges from 10% to 24% beneath the array. The S-to-P kernel recovers the center of the bump. However, the lateral extent of the bump is slightly exaggerated in comparison to its true scale using the analytical S-to-P kernel, with a more gradual return to zero. The S-to-P CCP stacking approach exaggerates the scale of the bump, slightly flattening it to more of a step shape. The recovered magnitude of the discontinuity using the S-to-P kernel ranges from 12% to 42% beneath the array.

The analytical P-to-S kernel resolves the structure of the deep undulating discontinuity at 100 km best (Figure 6g) in comparison to the analytical S-to-P kernel (Figure 7g) and also the CCP stacking approaches (Figures 6h and 7h). The P-to-S kernel recovers both the high and low topography and also the more vertical regions, near the

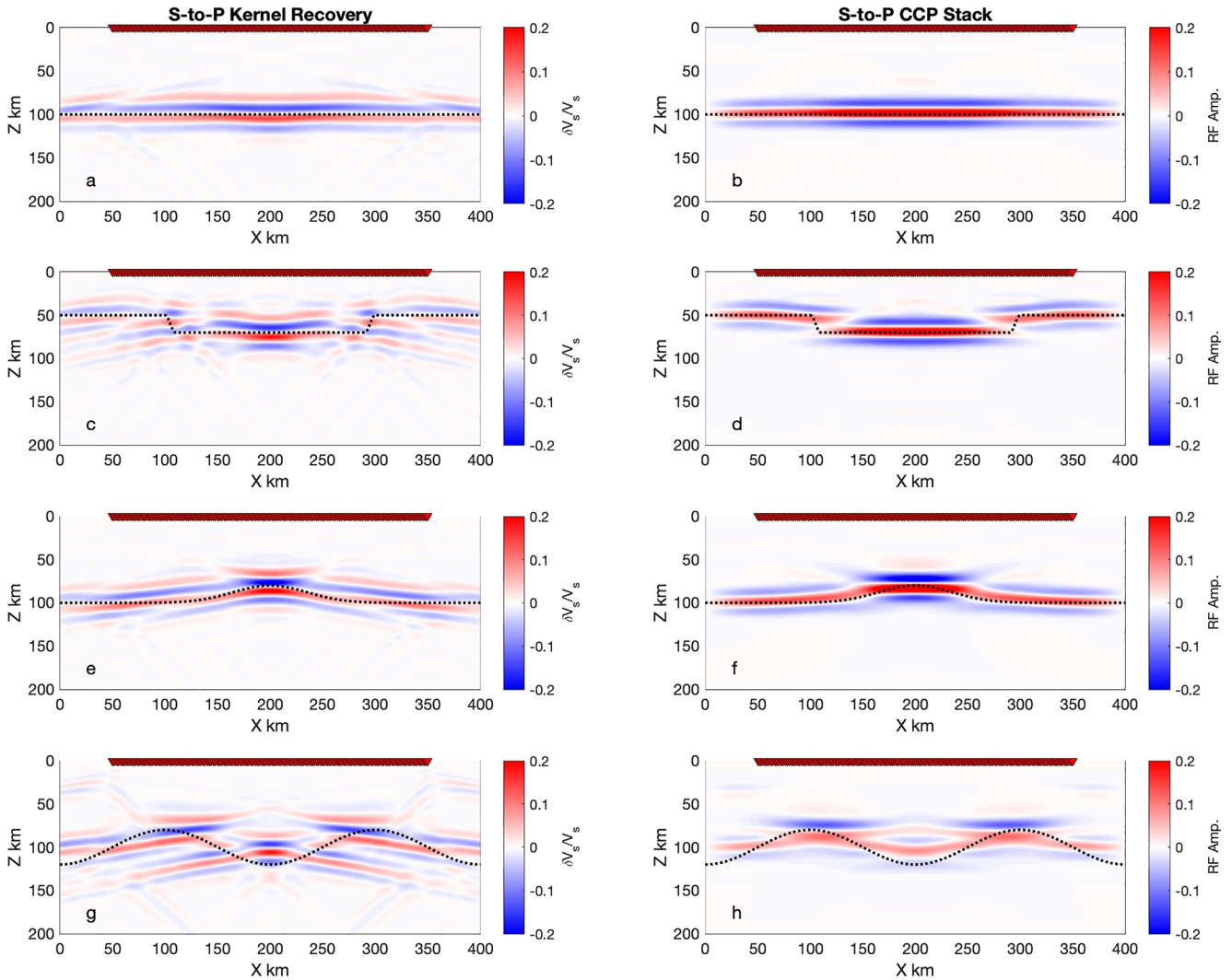

Figure 7. Recovery of velocity discontinuities at 50–120 km depth using analytical S-to-P kernels (left) in comparison to the common conversion point stacking approach (right). We present recovery of (a, b) a flat discontinuity at 100 km depth (c, d) a discontinuity with a step from 50 to 70 km depth over 20 km distance (e, f) a discontinuity at 100 km with a Gaussian bump with $\sigma = 35$ and amplitude 20 km in depth, and (g, h) sinusoidal topography centered at 100 km depth with amplitude of ±20 km and wavelength of 200 km.

zero crossings. The P-to-S CCP stacking approach does not recover the troughs. It recovers the peaks, but also artificially smears them laterally by almost 100 km on each side. There is some recovery of the vertical portions, although the recovery is artificially deep by 20 km. Amplitude recovery of the P-to-S kernel ranges from 14% to 34% within the well-recovered trough region in comparison to the 28% input model. The S-to-P kernel does not resolve the undulating discontinuity well, recovering discontinuities ∼15 km shallower than the deepest parts, with concave downward artificial tails. There is little or no recovery of the more vertical portions, and the shallowest portions are recovered as features dipping away from the shallow peaks toward the edges of the box. The S-to-P CCP stacking approach underestimates the depths of the deepest topography and overestimates the depth of the shallowest topography by 10–15 km. There are also artifacts related to horizontal smearing of the shallowest topography by up to 100 km. The magnitude of the S-to-P kernel recovery varies from 34% in the trough region to 24% near the peaks in comparison to the 28% input model.

The structure of the bump discontinuity at 30 km depth is well-resolved by the analytical P-to-S kernel (Figure 8a), the analytical S-to-P kernel (Figure 8e) and also the P-to-S and S-to-P CCP stacking approaches (Figures 8b and 8f) with minimal artifacts nearby the interface. The magnitude of the P-to-S kernel recovery ranges from

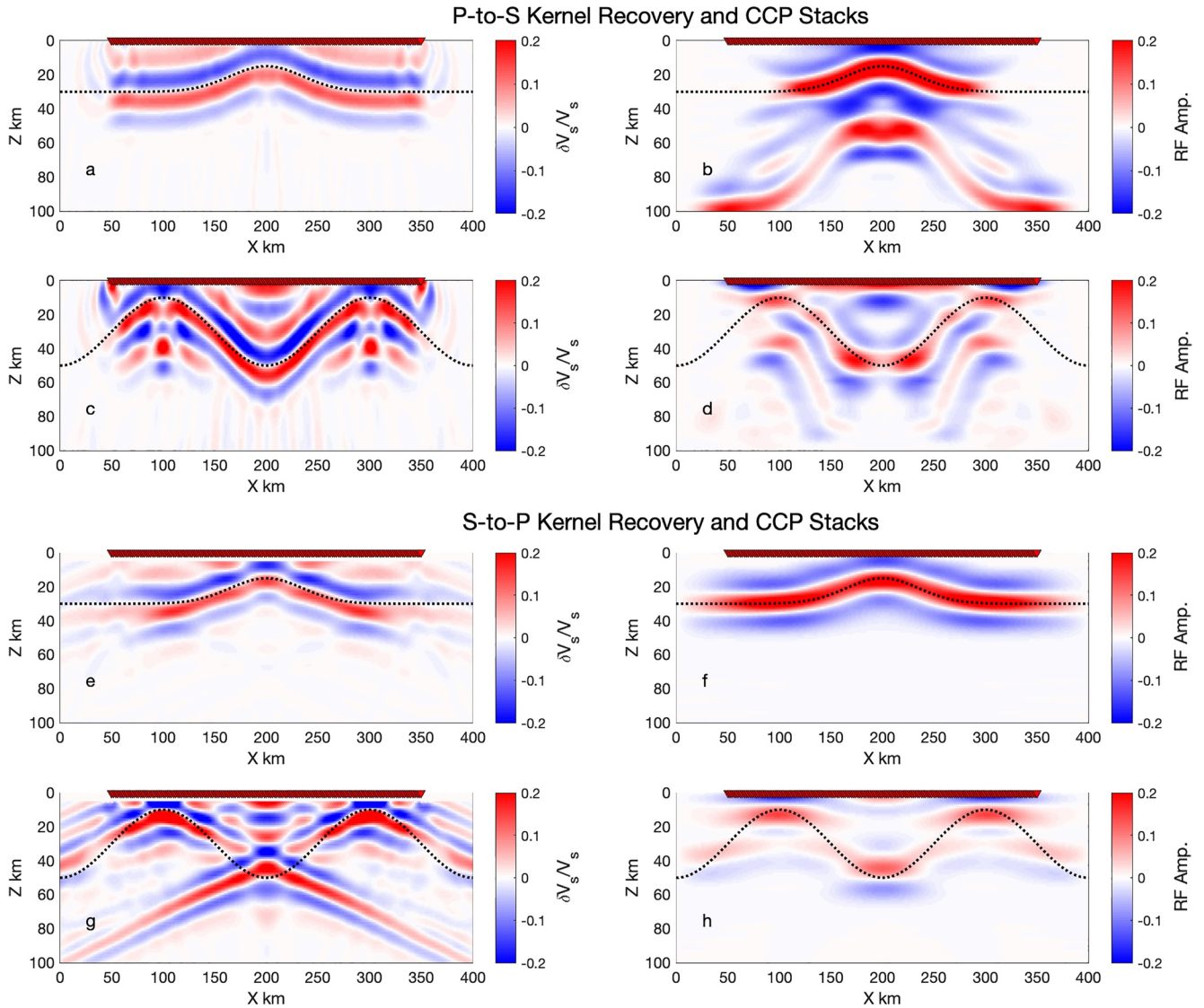

Figure 8. Recovery of velocity discontinuities at <50 km depth using analytical P-to-S and S-to-P kernels (left) in comparison to the common conversion point stacking approach (right). We present P-to-S recovery of (a, b) a discontinuity at 30 km depth with a Gaussian bump with $\sigma = 35$ km and amplitude of 15 km in depth, and (b, c) sinusoidal topography centered at 30 km depth with amplitude of ±20 km and wavelength of 200 km. We present S-to-P recovery of (e, f) a discontinuity at 30 km depth with a Gaussian bump with $\sigma = 35$ km and amplitude of 15 km in depth, and (g, h) sinusoidal topography centered at 30 km depth with amplitude of ±20 km and wavelength of 200 km.

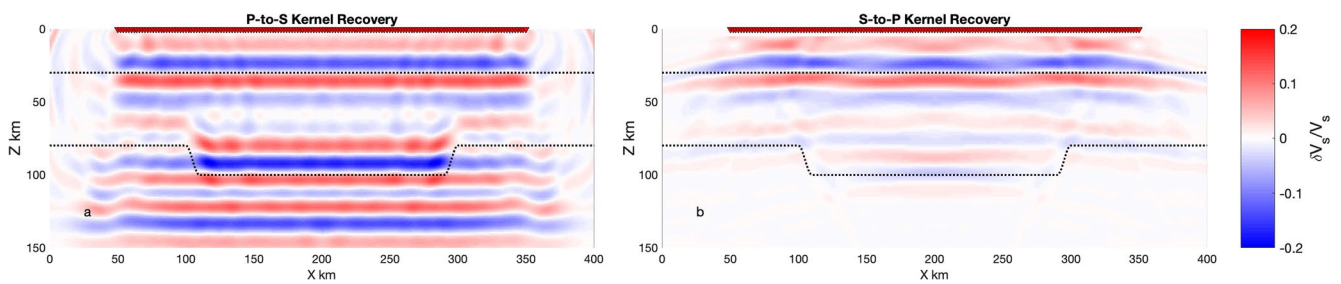

Figure 9. Recovery of secondary velocity discontinuities with a step, for example, the next discontinuity deeper than the Moho, such as a velocity decrease with depth at the lithosphere-asthenosphere boundary using analytical P-to-S and S-to-P kernels. The Moho is flat and located at 30 km depth. The example lithosphere-asthenosphere boundary discontinuity steps from 80 to 100 km depth over 20 km in distance. We present recovery for both (a) P-to-S and (b) S-to-P kernels.

20% to 27% in comparison to the 28% input model along the surface of the discontinuity beneath the array. The image recovered by the P-to-S kernel includes a deeper artificial bump that is caused by free-surface multiples. The P-to-S free-surface multiples arrive much later in the case where the discontinuity is at 100 km depth and therefore are not visible in the image. The S-to-P kernel recovers the shallow bump well, with minimal artifacts. The recovered magnitudes from the S-to-P kernel range from of 15%–32% along the bump region beneath the array in comparison to the 28% input model. The S-to-P CCP stacking approach recovers the bump discontinuity well, with no apparent artifacts.

The analytical P-to-S kernel resolves the shallow undulating discontinuity at 30 km depth best (Figure 8c) in comparison to the analytical S-to-P kernel (Figure 8g) and also the CCP stacking approaches (Figures 8d and 8h). The magnitude of the P-to-S kernel recovery ranges from 29% to 41% beneath the array. The P-to-S recovery is accompanied by later artifacts caused by free-surface multiples. The P-to-S CCP stacking approach resolves an undulating feature, albeit artificially flattened near the trough, over a ∼50 km wide area on either side. The S-to-P kernel resolves the shape of the undulating discontinuity at the shallowest peaks in the undulations but does not recover the more vertical portions or deepest portions. There are also additional artifacts at depth, that could potentially be cancelled with additional sources and/or receivers. There are also later artifacts caused by free-surface multiples. The magnitude of the S-to-P kernel recovery ranges from 10%–96% beneath the array. The S-to-P CCP stacking approach recovers discontinuities at the peaks and troughs of the undulations as artificially flat features, here 5–10 km wide, and does not resolve the more vertical portions.

The analytical P-to-S kernel recovers deep lithosphere-asthenosphere features beneath a Moho better than S-to-P (Figure 9). The P-to-S kernel recovers a step, both flat and vertical portions, albeit at artificially shallow depths (10–15 km). In addition, there are later arrivals of free-surface multiples. The P-to-S kernel recovers a velocity decrease with depth as large as 7% on the shallower parts and a decrease as large as 24% on the deeper parts relative to a 10% input model. The amplification of the deeper parts is caused by constructive interference with free-surface multiples. The S-to-P kernel also recovers faint artificial flat discontinuities at 15 km above the step. The S-to-P kernel recovers a contrast as large as 7% in comparison to the 10% input model. The S-to-P kernel does not recover the vertical portions of the step. In addition, there are artifacts where the shallow portions of the step smear artificially by 100 km into locations where the step is deeper.

3.3. Effects of Noise and Velocity Model Assumptions on Recovery

We test the effect of noise on the structural amplitude recovery by adding random Gaussian distributed noise to the synthetic seismograms calculated through the model including a negative Gaussian bump at 100 km depth (Figure 10). We test signal-to-noise ratios (SNR) of 1, 3, and 10 calculated relative to the converted phase amplitudes for P-to-S and S-to-P kernels. For all SNR the structural information is recovered; although, with a SNR of 1, there is a larger degree of speckle in the recovery (Figures 10a and 10b). For the P-to-S kernel the structure is also as clear as the noise-free synthetics at SNR of 3 and 10 (Figures 10c and 10e compared to Figure 6c). For the S-to-P kernel the structure is less continuous for a SNR of 3, and the structure is similar to the structure observed in the noise-free calculation for a SNR of 10 (Figures 10d and 10f compared to Figure 7c). The recovery of velocity contrast magnitudes is generally over-estimated for SNR of 1, with velocity contrasts of 30–40% for the P-to-S kernel and up to 180% for the S-to-P kernel relative to the input contrast of 28%. The velocity contrast estimate for SNR of 3 is as high as 37% for the P-to-S kernel and up to 43% for the S-to-P kernel, while at SNR of 10 the velocity contrasts are closer to the noise-free estimates at 23% for the P-to-S kernel and ranging from 14% to 40% for the S-to-P kernel. The over-estimate of the velocity contrasts in these models is due to the increase in the estimate of the misfit function caused by added noise and a corresponding increase in the scaling of the kernel. Windowing of the phase of interest may help to ameliorate this problem if it can be clearly identified.

We also test the case where the kernels are calculated using velocities 10% faster than reality for the case of the Gaussian bump at 100 km depth. We find that this impacts (increases) the absolute depth of the recovered discontinuity by 10%, as might be expected, but it does not have a large impact amplitude recovery, with <1%–2% difference than recovery assuming the correct velocity. In reality tomographic imaging could be used to provide a suitable velocity model for kernel calculation in a region that is relatively homogeneous laterally, and more sophisticated approaches would be needed in more heterogeneous regions.

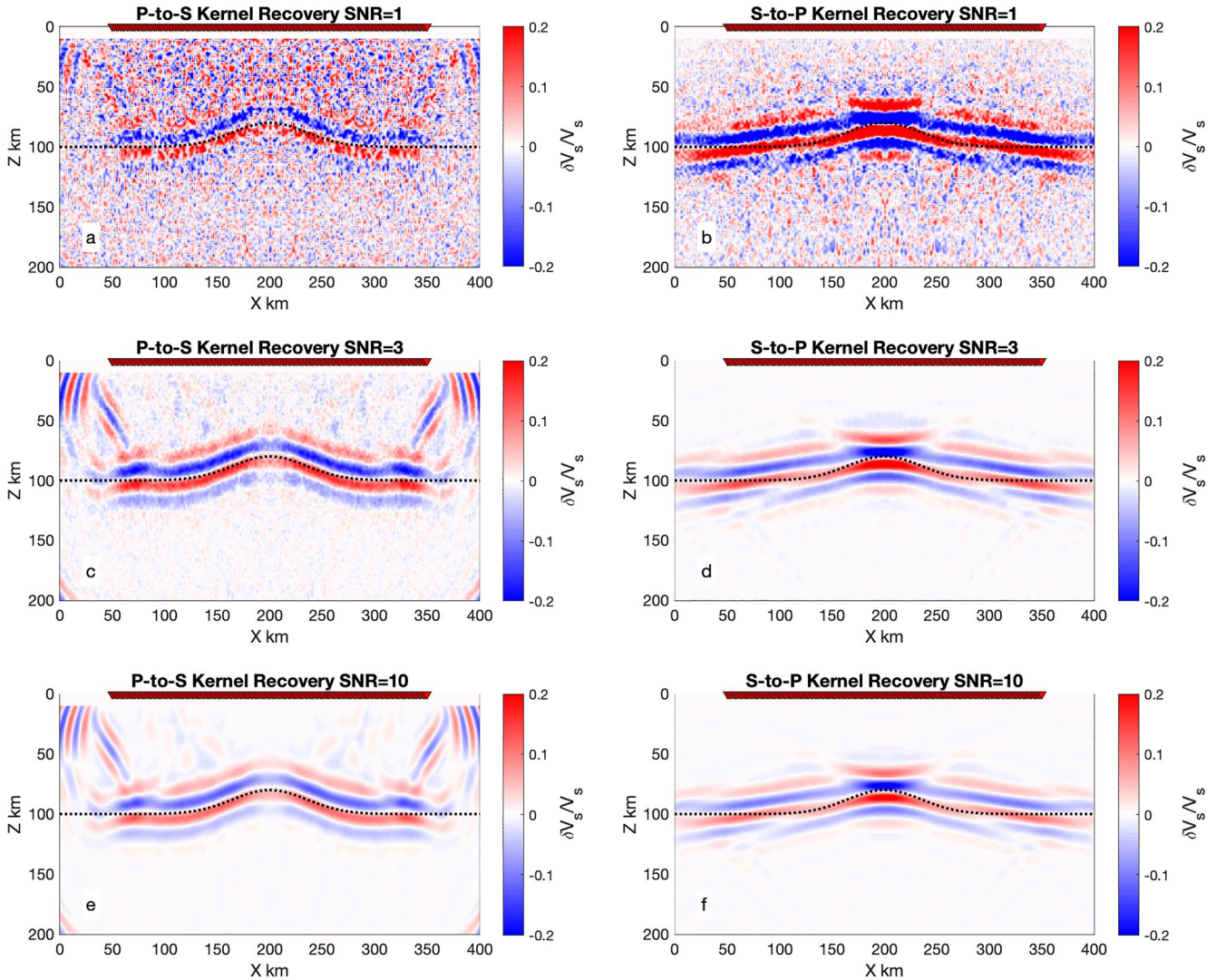

Figure 10. Effects of noise on recovery for P-to-S (left) and S-to-P (right) kernels for three different signal-to-noise ratios (SNR), including: (a, b) one, (b, c) three, and (e, f) ten. Depth and structure of the discontinuity are shown as dashed black lines. Red triangles show the locations of the stations used. SNR is calculated relative to the converted phase amplitude.

4. Discussion

4.1. Kernel Verification and Recovery

Our analytical kernels agree well with other results. Our kernels agree with those calculated using SEM both in shape and in amplitude (Figures 2–5). We find agreement in terms of the shapes of our kernels with previous studies that have explicitly calculated and presented P-to-S (Bogiatzis et al., 2022; Hansen & Schmandt, 2017) and S-to-P kernels (Bogiatzis et al., 2022; Hansen & Schmandt, 2017; Mancinelli & Fischer, 2018). The absolute amplitudes of the kernels presented in Figures 2–5) are the same as those in the work of Bogiatzis et al. (2022), but 3–5 orders of magnitude smaller than other previous results (Hansen & Schmandt, 2017; Mancinelli & Fischer, 2018). This is because the source and the adjoint source used to calculate the kernels in Figures 2–5 have been normalised. In addition, our choice of source wavelet normalization, dividing by the sum of the spectral amplitude, reduces the amplitude of the kernel. We do not need to multiply by a factor ∼1.10 to achieve a good agreement with the SEM kernels as required in the work of Mancinelli and Fischer (2018).

The P-to-S kernel recovers undulating topography at shallow and deep depths and steps better than the CCP stacking approach. The P-to-S kernel also recovers the bump at shallow depth as well as CCP stacking. The main

advantage of the P-to-S kernel is imaging the first discontinuity with depth, and structural recovery is generally good even with low SNR. The better P-to-S kernel recovery of dipping or undulating structures in comparison to S-o-P kernel recovery agrees with previous work using more sophisticated ray tracing approaches. The work of Hansen and Schmandt (2017) shows that the P-to-S kernel recovers discontinuities with steeper dips better than the S-to-P kernel. The work of Bogiatzis et al. (2022) also finds better recovery of sinusoidal and Gaussian shaped topography using P-to-S kernels in comparison to S-to-P kernels.

The P-to-S kernel is typically better at recovering shallow structure since it is complicated by multiples at greater depth. The P-to-S kernel has some potential for imaging topography on discontinuities deeper than the Moho, especially if free-surface multiples can be avoided by windowing. Our difficulties imaging secondary discontinuities, that is, beneath the shallowest Moho discontinuity, using P-to-S kernels is different than the findings of Hansen and Schmandt (2017) which reported good recovery of secondary features, discontinuities beneath the shallowest Moho discontinuity. This is likely caused by several reasons, including that the study includes: (a) finer station spacing (1 km in comparison to 2 km), (b) additional sources (10 in comparison to 4), (c) a higher frequency wave (1.25 s in comparison to 4 s), (d) a more sophisticated ray tracing method, that is, fast marching through the known velocity structure in the calculation of the kernels, and (e) possibly more sophisticated phase windowing.

The S-to-P kernel is better at recovering discontinuities at shallow depths in comparison to deep depths. In typical CCP stacking approaches S-to-P is more useful than P-to-S for imaging discontinuities deeper than the Moho, given that the converted S-to-P arrives before the S-wave and Moho multiples are avoided (Li et al., 2004; Rychert et al., 2007). The poor S-to-P recovery of the deeper discontinuity structure could be related to the fact that the kernel calculation used here presumes a fixed incidence angle of the source wavefield, which is not correct in the presence of dipping layers, which can lead to greater errors with increasing depth. Alternatively, it could be related to the smaller number of stacked kernels at depth owing to the size of the array, which could be ameliorated by increasing the array aperture (Mancinelli & Fischer, 2018; Rondenay et al., 2005). Better recovery of shallow structures by S-to-P kernels is also reported in the work of Mancinelli and Fischer (2018) and the work of Hansen and Schmandt (2017).

The S-to-P kernel does not recover topography as well as the P-to-S kernel or CCP stacking approach in general. Structural recovery is similar at all SNR for the S-to-P kernel although the number of artifacts at low SNR suggests interpretation may be difficult. The most promising aspect of the S-to-P kernel is that it can recover the shallow curvature of large undulations with amplitude of $\pm$20 km that would otherwise appear as artificially flat features in CCP stacking (Figures 8g and 8h). Therefore, in locations where CCP stacking images steps in the Moho the S-to-P kernel could be used to evaluate whether there is curvature on the discontinuity steps. In other words, it is a simple additional test, if already using S-to-P, that does not involve processing a new P-to-S data set or a more computationally intensive approach.

Structural recovery using our analytical kernels is similar or worse than that of another study that used the same station and event set-up and some of the same discontinuity structures (Bogiatzis et al., 2022). For instance, our P-to-S and S-to-P kernels recover the Gaussian bump just as well as the previous work. Recovery of the sinusoidal topography using the P-to-S kernel is the same near the center of the array, with worse recovery toward the edges of the array in comparison to the previous work. Our recovery of the sinusoidal topography using the analytical S-to-P kernel has more artifacts in comparison to the previous work. In addition, the analytical S-to-P kernel recovers the trough in the center of the array 15 km shallower than the true model; whereas, the central trough was recovered at the correct depth in the previous work. These differences are likely because the work of Bogiatzis et al. (2022) used a more sophisticated ray tracing approach to calculate the kernels.

The observed variability in amplitude recovery agrees with previous work. The work of Bogiatzis et al. (2022) inverted for the magnitude of the velocity contrast and also found recovery that was both smaller and larger than the true model. The work of Mancinelli and Fischer (2018) similarly reported variability of scattering potential, a proxy for amplitude variation based on comparing lithosphere-asthenosphere amplitudes to overlying Moho amplitudes in a kernel stack. The observed range of amplitude recovery likely arises from the effects of focusing and defocusing, which results in variable kernel cancellation, and in the case of P-to-S interference with later arriving free-surface multiples.

The amplitude recovery of the P-to-S and S-to-P kernels is typically within 10% of the input model values. However, sections of the discontinuities are both under and over predicted by both P-to-S and S-to-P. The range of the amplitudes recovered by the P-to-S kernel for a given discontinuity is typically smaller than that recovered by the S-to-P kernel in almost all cases. The P-to-S kernel has the best amplitude recovery in the case of the step and the shallow bump. Overall, the results suggest that a reasonable estimate of the velocity contrast of the discontinuity might be derived from the analytical kernels, but some caution should be employed in interpreting variations in the strength of the discontinuities due to the focusing and interference effects. This is especially true if the SNR is relatively low, as the increased noise levels result in greater variability and a greater potential for over-estimating the velocity contrast. Median or average values along a given discontinuity may provide a more robust estimate of the velocity contrast in the presence of topography.

4.2. Computational Cost

Using a 2.2 GHz Intel core i7 and an unoptimized MATLAB code (no parallelization) the analytical kernel calculation for a single plane wave source is very fast << 1 s for a 400 km by 200 km domain, sampled at 1 km. The calculation needs to be performed for each plane wave source, but because our homogenous medium is symmetric, it only needs to be performed on one side of the model and reflected along a vertical symmetry axis to include sources on the other side. To generate the stacked kernel, for a single plane wave source including processing and stacking of 151 stations seismograms takes ∼3 s. Most of the cost is from multiplying the Fourier coefficients with the kernel, summing over frequency and then interpolation from station centered coordinates onto the global coordinates, which can be parallelized and optimized further.

For comparison, previous work using more sophisticated ray tracing approaches to account for velocity heterogeneity require more computational time. The work of Hansen and Schmandt (2017) uses a single CPU Linux machine and Matlab (8 core AMD processor, 32 GB RAM) and requires 2 hr to calculate the traveltime fields for 443 stations (about 3 times the number of stations used here) and a similar sized region (465 × 250 km) and a fast marching approach. Stacking the kernels requires about 20 s per event. Hansen and Schmandt (2017) also find that the GRT inversion (Bostock et al., 2001) takes 80 min for 10 sources and 443 stations or an average of 8 min per event. In another comparison, the work of Bogiatzis et al. (2022) requires 1,525 s for the same model set up used here on one CPU core of an ordinary laptop computer (i7-8850U 1.8 Ghz with 16 GB of main memory). The computational time requires a few seconds for the grid and forward and adjoint matrices as well as an additional ∼3 s for every source (two sources were used, given symmetry), and ∼10 s for every station.

The computational costs of using the SEM are at least two orders of magnitude different than using the analytical kernel. The full-waveform forward simulation takes about 491 s using four CPU cores (Intel(R) Core(TM) i7-7700 CPU @ 3.60 GHz). Using the same computational setup, the full-waveform simulation for the layered half-space takes about the same computational time as for the homogeneous case, ∼500 s. The adjoint simulation takes a similar time. So for a single source kernel the total time is approximately 1,000 s. Computational costs for the SEM can be reduced by about one order of magnitude when using a grid spacing of 1 km.

5. Conclusions

We present 2-D analytical P-to-S and S-to-P scattered wave finite frequency kernels and evaluate their accuracy and computational cost. The kernels compare favorably with those calculated using SPECFEM2D. The kernels are computationally efficient taking << 1 s to calculate. We find that the analytical P-to-S kernel is an effective and rapid tool for recovering shallow discontinuity structure including sharp dips and strong curvature. The analytical S-to-P kernel is not well-suited to topography recovery. However, in locations where strong steps are imaged by CCP stacking, the S-to-P kernel may be used to constrain the curvature. In addition, despite some variability in the recovered amplitudes, the kernels can provide an estimate of the magnitude of the velocity change at depth, without requiring additional waveform modeling.

Data Availability Statement

No data were used in this manuscript. Models and kernels for the SEM are computed via the open-source codes SPECFEM2D (https://github.com/geodynamics/specfem2d). The analytical kernel codes used here are included with the manuscript in Supporting Information S1 and S2.

Acknowledgments
We acknowledge funding from the Natural Environment Research Council (NE/M003507/1) and the European Research Council (GA 638665) for supporting this work. We thank Qinya Liu and Tianshi Liu for discussions about the units of the SEM kernels.

References

Agius, M., Harmon, N., Rychert, C. A., Tharimena, S., & Kendall, J. M. (2018). Sediment characterization at the equatorial mid-Atlantic ridge from P-to-S teleseismic phase conversions recorded on the PI-LAB experiment. *Geophysical Research Letters*, *45*(22), 12244–12252. https://doi.org/10.1029/2018GL080565

Agius, M., Rychert, C. A., Harmon, N., Kendall, J. M., & Tharimena, S. (2021). A thin mantle transition zone beneath the equatorial Mid-Atlantic Ridge. *Nature*, *589*(7843), 562–566. https://doi.org/10.1038/s41586-020-03139-x

Agius, M. R., Rychert, C. A., Harmon, N., & Laske, G. (2017). Mapping the mantle transition zone beneath Hawaii from Ps receiver functions: Evidence for a hot plume and cold mantle downwellings. *Earth and Planetary Science Letters*, *474*, 226–236. https://doi.org/10.1016/j.epsl.2017.06.033

Angus, D. A., Kendall, J. M., Wilson, D. C., White, D. J., Sol, S., & Thomson, C. J. (2009). Stratigraphy of the Archean Western Superior Province from P- and S-wave receiver functions: Further evidence for tectonic accretion?*Physics of the Earth and Planetary Interiors*, *177*(3–4), 206–216. https://doi.org/10.1016/j.pepi.2009.09.002

Armitage, J. J., Ferguson, D. J., Goes, S., Hammond, J. O. S., Calais, E., Rychert, C. A., & Harmon, N. (2015). Upper mantle temperature and the onset of extension and break-up in Afar, Africa. *Earth and Planetary Science Letters*, *418*, 78–90. https://doi.org/10.1016/j.epsl.2015.02.039

Audet, P. (2016). Receiver functions using OBS data: Promises and limitations from numerical modelling and examples from the Cascadia initiative. *Geophysical Journal International*, *205*(3), 1740–1755. https://doi.org/10.1093/gji/ggw111

Bank, C. G., & Bostock, M. G. (2003). Linearized inverse scattering of teleseismic waves for anisotropic crust and mantle structure: 2. Numerical examples and application to data from Canadian stations. *Journal of Geophysical Research*, *108*. https://doi.org/10.1029/2002jb001951

Bogiatzis, P., Rychert, C. A., & Harmon, N. (2021). Multiple graph realizations method: Improving the accuracy and the efficiency of the shortest path method through random sampling. *Geophysical Journal International*, *227*(1), 669–679. https://doi.org/10.1093/gji/ggab247

Bogiatzis, P., Rychert, C. A., Harmon, N., & Xie, Y. (2022). Fast calculation of spatial sensitivity kernels for converted waves in arbitrary heterogeneous media using graph theory. *Geophysical Journal International*, *230*(1), 654–672. https://doi.org/10.1093/gji/ggac078

Bostock, M. G. (1998). Mantle stratigraphy and evolution of the Slave province. *Journal of Geophysical Research*, *103*, 21183–21200. https://doi.org/10.1029/98JB01069

Bostock, M. G., Rondenay, S., & Shragge, J. (2001). Multiparameter two-dimensional inversion of scattered teleseismic body waves 1. Theory for oblique incidence. *Journal of Geophysical Research*, *106*(B12), 30771–30782. https://doi.org/10.1029/2001JB000330

Chambers, E. L., Harmon, N., Keir, D., & Rychert, C. A. (2019). Using ambient noise to image the northern east African rift. *Geochemistry, Geophysics, Geosystems*, *20*(4), 2091–2109. https://doi.org/10.1029/2018gc008129

Chambers, E. L., Harmon, N., Rychert, C. A., & Keir, D. (2021). Variations in melt emplacement beneath the northern East African Rift from radial anisotropy. *Earth and Planetary Science Letters*, *573*, 117150. https://doi.org/10.1016/j.epsl.2021.117150

Chen, L., Wen, L. X., & Zheng, T. Y. (2005). A wave equation migration method for receiver function imaging: 2. Application to the Japan subduction zone. *Journal of Geophysical Research*, *110*. https://doi.org/10.1029/2005jb003666

Cheng, C., Bodin, T., & Allen, R. M. (2016). Three-dimensional pre-stack depth migration of receiver functions with the fast marching method: A Kirchhoff approach. *Geophysical Journal International*, *205*(2), 819–829. https://doi.org/10.1093/gji/ggw062

Chichester, B., Rychert, C., Harmon, N., van der Lee, S., Frederiksen, A., & Zhang, H. (2018). Seismic imaging of the North American midcontinent rift using S-to-P receiver functions. *Journal of Geophysical Research*, *123*(9), 7791–7805. https://doi.org/10.1029/2018jb015771

Chichester, B., Rychert, C. A., Harmon, N., Rietbrock, A., Collier, J., Henstock, T. J., & Goes, S. (2020). Sediment characterisation beneath the VOILA experiment in the Lesser Antilles from P-to-S conversions. *Geophysical Journal International*, *223*(3), 1758–1768. https://doi.org/10.1093/gji/ggaa360

Cooper, G. F., Macpherson, C. G., Blundy, J. D., Maunder, B., Allen, R. W., Goes, S., et al. (2020). Variable water input controls evolution of the Lesser Antilles volcanic arc. *Nature*, *584*(7822), 525–529. https://doi.org/10.1038/s41586-020-2582-4

Dahlen, F. A., Hung, S. H., & Nolet, G. (2000). Frechet kernels for finite-frequency traveltimes - I. Theory. *Geophysical Journal International*, *141*(1), 157–174. https://doi.org/10.1046/j.1365-246X.2000.00070.x

Dijkstra, E. W. (1959). A note on two problem in connexion with graphs. *Numerische Mathematik*, *1*, 269–271. https://doi.org/10.1007/BF01386390

Dueker, K. G., & Sheehan, A. F. (1997). Mantle discontinuity structure from midpoint stacks of converted P to S waves across the Yellowstone hotspot track. *Journal of Geophysical Research*, *102*, 8313–8327. https://doi.org/10.1029/96jb03857

Eakin, C., Rychert, C. A., & Harmon, N. (2018). Flow beneath mid-ocean ridges from source side shear wave splitting. *Journal of Geophysical Research*, *123*(2), 1736–1751. https://doi.org/10.1002/2017JB015176

Ford, H. A., Fischer, K. M., Abt, D. L., Rychert, C. A., & Elkins-Tanton, L. T. (2010). The lithosphere-asthenosphere boundary and cratonic lithospheric layering beneath Australia from Sp wave imaging. *Earth and Planetary Science Letters*, *300*(3–4), 299–310. https://doi.org/10.1016/j.epsl.2010.10.007

Hammond, J. O. S., Kendall, J. M., Stuart, G. W., Keir, D., Ebinger, C., Ayele, A., & Belachew, M. (2011). The nature of the crust beneath the Afar Triple Junction: Evidence from receiver functions. *Geochemistry, Geophysics, Geosystems*, *12*, Q12004. https://doi.org/10.1029/2011GC003738

Hansen, S. M., & Schmandt, B. (2017). P and S wave receiver function imaging of subduction with scattering kernels. *Geochemistry, Geophysics, Geosystems*, *18*(12), 4487–4502. https://doi.org/10.1002/2017gc007120

Harmon, N., Gerstoft, P., Rychert, C. A., Abers, G. A., dela Cruz, M. S., & Fischer, K. M. (2008). Phase velocities from seismic noise using beamforming and cross correlation in Costa Rica and Nicaragua. *Geophysical Research Letters*, *35*(19), L19303. https://doi.org/10.1029/2008gl035387

Harmon, N., & Rychert, C. A. (2015). Seismic imaging of deep crustal melt sills beneath Costa Rica suggests a method for the formation of the Archean continental crust. *Earth and Planetary Science Letters*, *430*, 140–148. https://doi.org/10.1016/j.epsl.2015.07.062

Harmon, N., Rychert, C. A., Agius, M. R., Tharimena, S., Le Bas, T. P., Kendall, J. M., & Constable, S. (2018). Marine geophysical investigation of the chain fracture zone in the equatorial Atlantic from the PI-LAB experiment. *Journal of Geophysical Research*, *123*(12), 11016–11030. https://doi.org/10.1029/2018jb015982

Harmon, N., Rychert, C. A., Goes, S., Maunder, B., Collier, J., Henstock, T., et al. (2021a). Widespread hydration of the back arc and the link to variable hydration of the incoming plate in the Lesser Antilles from Rayleigh Wave Imaging. *Geochemistry, Geophysics, Geosystems*, *22*(7), e2021GC009707. https://doi.org/10.1029/2021GC009707

Harmon, N., Rychert, C. A., Kendall, J., Tharimena, S., Bogiatzis, P., & Agius, M. (2020). Evolution of the oceanic lithosphere in the equatorial Atlantic from Rayleigh Wave tomography, evidence for small-scale convection from the PI-LAB experiment. *Geochemistry, Geophysics, Geosystems*, *21*(9), e2020GC009174. https://doi.org/10.1029/2020GC009174

Harmon, N., Salas De La Cruz, M., Rychert, C. A., Fischer, K. M., & Abers, G. A. (2013). Crustal and mantle shear velocity structure of Costa Rica and Nicaragua from ambient noise and teleseismic Rayleigh wave tomography. *Geophysical Journal International*, *195*(2), 1300–1313. https://doi.org/10.1093/gji/ggt309

Harmon, N., Wang, S., Rychert, C. A., Constable, S., & Kendall, J. M. (2021b). Shear velocity inversion guided by resistivity structure from the PI-LAB Experiment for integrated estimates of partial melt in the mantle. *Journal of Geophysical Research*, *126*. https://doi.org/10.1002/essoar.10506813.1

Hua, J. L., Fischer, K. M., Mancinelli, N. J., & Bao, T. Z. (2020). Imaging with pre-stack migration based on Sp scattering kernels. *Geophysical Journal International*, *220*(1), 428–449. https://doi.org/10.1093/gji/ggz459

Komatitsch, D., Vilotte, J. P., Cristini, P., Labarta, J., Le Goff, N., Le Loher, P., et al. (2012). *SPECFEM2D v7.0.0, computational infrastructure for geodynamics*. https://geodynamics.org/cig/software/specfem2d/

Lavayssiere, A., Rychert, C., Harmon, N., Keir, D., Hammond, J. O. S., Kendall, J. M., et al. (2018). Imaging lithospheric discontinuities beneath the northern East African Rift using S-to-P receiver functions. *Geochemistry, Geophysics, Geosystems*, *19*(10), 4048–4062. https://doi.org/10.1029/2018gc007463

Lawrence, J. F., & Shearer, P. M. (2006). A global study of transition zone thickness using receiver functions. *Journal of Geophysical Research*, *111*. https://doi.org/10.1029/2005jb003973

Lekic, V., & Fischer, K. M. (2017). Interpreting spatially stacked Sp receiver functions. *Geophysical Journal International*, *210*(2), 874–886. https://doi.org/10.1093/gji/ggx206

Lekic, V., French, S. W., & Fischer, K. M. (2011). Lithospheric thinning beneath rifted regions of southern California. *Science*, *334*(6057), 783–787. https://doi.org/10.1126/science.1208898

Leng, K. D., Nissen-Meyer, T., & van Driel, M. (2016). Efficient global wave propagation adapted to 3-D structural complexity: A pseudospectral/spectral-element approach. *Geophysical Journal International*, *207*(3), 1700–1721. https://doi.org/10.1093/gji/ggw363

Leng, K. D., Nissen-Meyer, T., van Driel, M., Hosseini, K., & Al-Attar, D. (2019). AxiSEM3D: Broad-band seismic wavefields in 3-D global Earth models with undulating discontinuities. *Geophysical Journal International*, *217*(3), 2125–2146. https://doi.org/10.1093/gji/ggz092

Levander, A. (2003). USArray design implications for wavefield imaging in the lithosphere and upper mantle. *The Leading Edge*, *22*(3), 250–255. https://doi.org/10.1190/1.1564530

Levander, A., Niu, F. L., Lee, C. T. A., & Cheng, X. (2006). Imag(in)ing the continental lithosphere. *Tectonophysics*, *416*(1–4), 167–185. https://doi.org/10.1016/j.tecto.2005.11.018

Li, X. Q., Kind, R., Yuan, X. H., Wolbern, I., & Hanka, W. (2004). Rejuvenation of the lithosphere by the Hawaiian plume. *Nature*, *427*(6977), 827–829. https://doi.org/10.1038/nature02349

Ligorria, J. P., & Ammon, C. J. (1999). Iterative deconvolution and receiver-function estimation. *Bulletin of the Seismological Society of America*, *89*(5), 1395–1400. https://doi.org/10.1785/BSSA0890051395

Liu, K. J., & Levander, A. (2013). Three-dimensional Kirchhoff-approximate generalized Radon transform imaging using teleseismic P-to-S scattered waves. *Geophysical Journal International*, *192*(3), 1196–1216. https://doi.org/10.1093/gji/ggs073

Liu, Q. Y., & Tromp, J. (2006). *Finite-frequency kernels based on adjoint methods* (Vol. 96, pp. 2383–2397). B Seismol Soc Am. https://doi.org/10.1785/0120060041

Mancinelli, N. J., & Fischer, K. M. (2018). The spatial sensitivity of Sp converted waves—Scattered-wave kernels and their applications to receiver-function migration and inversion. *Geophysical Journal International*, *212*(3), 1722–1735. https://doi.org/10.1093/gji/ggx506

Millet, F., Bodin, T., & Rondenay, S. (2019). Multimode 3-D Kirchhoff migration of receiver functions at continental scale. *Journal of Geophysical Research*, *124*(8), 8953–8980. https://doi.org/10.1029/2018jb017288

Monteiller, V., Chevrot, S., Komatitsch, D., & Fuji, N. (2013). A hybrid method to compute short-period synthetic seismograms of teleseismic body waves in a 3-D regional model. *Geophysical Journal International*, *192*(1), 230–247. https://doi.org/10.1093/gji/ggs006

Monteiller, V., Chevrot, S., Komatitsch, D., & Wang, Y. (2015). Three-dimensional full waveform inversion of short-period teleseismic wavefields based upon the SEM-DSM hybrid method. *Geophysical Journal International*, *202*(2), 811–827. https://doi.org/10.1093/gji/ggv189

Nissen-Meyer, T., van Driel, M., Stähler, S. C., Hosseini, K., Hempel, S., Auer, L., et al. (2014). AxiSEM: Broadband 3-D seismic wavefields in axisymmetric media. *Solid Earth*, *5*(1), 425–445. https://doi.org/10.5194/se-5-425-2014

Owens, T. J., & Zandt, G. (1985). The response of the continental crust-mantle boundary observed on broad-band teleseismic receiver functions. *Geophysical Research Letters*, *12*(10), 705–708. https://doi.org/10.1029/GL012i010p00705

Park, J., & Levin, V. (2000). Receiver functions from multiple-taper spectral correlation estimates. *Bulletin of the Seismological Society of America*, *90*(6), 1507–1520. https://doi.org/10.1785/0119990122

Pearce, F. D., Rondenay, S., Sachpazi, M., Charalampakis, M., & Royden, L. H. (2012). Seismic investigation of the transition from continental to oceanic subduction along the Western Hellenic Subduction Zone. *Journal of Geophysical Research*, *117*, B07306. https://doi.org/10.1029/2011jb009023

Poppeliers, C., & Pavlis, G. L. (2003a). Three-dimensional, prestack, plane wave migration of teleseismic P-to-S converted phases: 1. Theory. *Journal of Geophysical Research*, *108*(B2). https://doi.org/10.1029/2001jb000216

Poppeliers, C., & Pavlis, G. L. (2003b). Three-dimensional, prestack, plane wave migration of teleseismic P-to-S converted phases: 2. Stacking multiple events. *Journal of Geophysical Research*, *108*(B5). https://doi.org/10.1029/2001jb001583

Possee, D., Rychert, C. A., Harmon, N., & Keir, D. (2021). Seismic discontinuities across the North American Caribbean plate boundary from S-to P- receiver functions. *Geochemistry, Geophysics, Geosystems*, *22*(7), e201GC009723. https://doi.org/10.1029/2021GC009723

Rondenay, S., Abers, G. A., & Van Keken, P. E. (2008). Seismic imaging of subduction zone metamorphism. *Geology*, *36*(4), 275–278. https://doi.org/10.1130/G24112a.1

Rondenay, S., Bostock, M. G., & Fischer, K. M. (2005). Multichannel inversion of scattered teleseismic body waves: Practical considerations and applicability. In A.Levander & G.Nolet(Eds.), *Seismic Earth: Array analysis of braodband seismograms, geophys. Mono. Ser.* AGU. https://doi.org/10.1029/157GM12

Rondenay, S., Bostock, M. G., & Shragge, J. (2001). Multiparameter two-dimensional inversion of scattered teleseismic body waves 3. Application to the Cascadia 1993 data set. *Journal of Geophysical Research*, *106*(B12), 30795–30807. https://doi.org/10.1029/2000JB000039

Rychert, C. A., Fischer, K. M., Abers, G. A., Plank, T., Syracuse, E., Protti, J. M., et al. (2008). Strong along-arc variations in attenuation in the mantle wedge beneath Costa Rica and Nicaragua. *Geochemistry, Geophysics, Geosystems*, *9*(10). https://doi.org/10.1029/2008GC002040

Rychert, C. A., Fischer, K. M., & Rondenay, S. (2005). A sharp lithosphere-asthenosphere boundary imaged beneath eastern North America. *Nature*, *436*(7050), 542–545. https://doi.org/10.1038/nature03904

Rychert, C. A., Hammond, J. O. S., Harmon, N., Kendall, J. M., Keir, D., Ebinger, C., et al. (2012). Volcanism in the Afar Rift sustained by decompression melting with minimal plume influence. *Nature Geoscience*, *5*(6), 406–409. https://doi.org/10.1038/Ngeo1455

Rychert, C. A., Harmon, N., & Armitage, J. (2018). Seismic imaging of thickened lithosphere resulting from plume pulsing beneath Iceland. *Geochemistry, Geophysics, Geosystems*, *19*(6), 1789–1799. https://doi.org/10.1029/2018gc00750

Rychert, C. A., Harmon, N., Constable, S., Wang, S., (2020). The nature of the lithosphere-asthenosphere boundary. *Journal of Geophysical Research*, *125*(10), e2018JB016463. https://doi.org/10.1029/2018JB016463

Rychert, C. A., Rondenay, S., & Fischer, K. M. (2007). P-to-S and S-to-P imaging of a sharp lithosphere-asthenosphere boundary beneath eastern North America. *Journal of Geophysical Research*, *112*, B08314. https://doi.org/10.1029/2006JB004619

Rychert, C. A., & Shearer, P. M. (2009). A global view of the lithosphere-asthenosphere boundary. *Science*, *324*(5926), 495–498. https://doi.org/10.1126/science.1169754

Rychert, C. A., Tharimena, S., Harmon, N., Kendall, J. M., Constable, S., Wang, S., et al. (2021). A dynamic tectonic lithosphere-asthenosphere boundary at the equatorial Mid-Atlantic Ridge. *Earth and Planetary Science Letters*, *566*, 116949. https://doi.org/10.1016/j.epsl.2021.116949

Saikia, U., Rychert, C. A., Harmon, N., & Kendall, J. M. (2021a). Seismic attenuation at the equatorial Mid-Atlantic Ridge constrained by local Rayleigh wave analysis from the PI-LAB experiment. *Geochemistry, Geophysics, Geosystems*, *22*(12). https://doi.org/10.1029/2021GC010085

Saikia, U., Rychert, C. A., Harmon, N., & Kendall, J. M. (2021b). Upper mantle anisotropic shear velocity structure at the equatorial Mid-Atlantic Ridge constrained by Rayleigh wave group velocity analysis from the PI-LAB experiment. *Geochemistry, Geophysics, Geosystems*, *22*(3). https://doi.org/10.1029/2020GC009495

Sanchezsesma, F. J., & Campillo, M. (1991). *Diffraction of P, Sv, and Rayleigh-Waves by Topographic Features - A Boundary Integral Formulation* (Vol. 81, pp. 2234–2253). B Seismol Soc Am. https://doi.org/10.1785/BSSA0810062234

Schlaphorst, D., Harmon, N., Kendall, J. M., Rychert, C. A., Collier, J., Rietbrock, A., Goes, S., & the VoiLA Team. (2021). Variation in crustal and upper mantle structure in the Greater and Lesser Antilles from ambient noise tomography. *Geochemistry, Geophysics, Geosystems*, *22*, (7), e2021GC009800. https://doi.org/10.1029/2021GC009800

Schulte-Pelkum, V., Monsalve, G., Sheehan, A., Pandey, M. R., Sapkota, S., Bilham, R., & Wu, F. (2005). Imaging the Indian subcontinent beneath the HSimalaya. *Nature*, *435*(7046), 1222–1225. https://doi.org/10.1038/nature03678

Sethian, J. A. (1996). A fast marching level set method for monotonically advancing fronts. *Proceedings of the National Academy of Sciences*, *93*(4), 1591–1595. https://doi.org/10.1073/pnas.93.4.1591

Sheehan, A. F., Shearer, P. M., Gilbert, H. J., & Dueker, K. G. (2000). Seismic migration processing of P-SV converted] phases for mantle discontinuity structure beneath the Snake River Plain, Western United States. *Journal of Geophysical Research*, *105*(B8), 19055–19065. https://doi.org/10.1029/2000jb900112

Shen, Y., Solomon, S. C., Bjarnason, I. T., & Wolfe, C. J. (1998). Seismic evidence for a lower-mantle origin of the Iceland plume. *Nature*, *395*(6697), 62–65. https://doi.org/10.1038/25714

Shragge, J., Bostock, M. G., & Rondenay, S. (2001). Multiparameter two-dimensional inversion of scattered teleseismic body waves 2. Numerical examples. *Journal of Geophysical Research*, *106*(B12), 30783–30793. https://doi.org/10.1029/2001JB000326

Syracuse, E. M., Abers, G. A., Fischer, K., MacKenzie, L., Rychert, C., Protti, M., et al. (2008). Seismic tomography and earthquake locations in the Nicaraguan and Costa Rican upper mantle. *Geochemistry, Geophysics, Geosystems*, *9*(7). https://doi.org/10.1029/2008gc001963

Tauzin, B., Debayle, E., & Wittlinger, G. (2008). The mantle transition zone as seen by global pds phases: No clear evidence for a thin transition zone beneath hotspots. *Journal of Geophysical Research*, *113*(B8). https://doi.org/10.1029/2007JB005364

Tong, P., Chen, C. W., Komatitsch, D., Basini, P., & Liu, Q. Y. (2014a). High-resolution seismic array imaging based on an SEM-FK hybrid method. *Geophysical Journal International*, *197*(1), 369–395. https://doi.org/10.1093/gji/ggt508

Tong, P., Komatitsch, D., Tseng, T. L., Hung, S. H., Chen, C. W., Basini, P., & Liu, Q. Y. (2014b). A 3-D spectral-element and frequency-wave number hybrid method for high-resolution seismic array imaging. *Geophysical Research Letters*, *41*(20), 7025–7034. https://doi.org/10.1002/2014gl061644

Tromp, J., Komatitsch, D., & Liu, Q. Y. (2008). Spectral-element and adjoint methods in seismology. *Communications in Computational Physics*, *3*, 1–32.

Tromp, J., Tape, C., & Liu, Q. (2005). Seismic tomography, adjoint methods, time reversal and banana-doughnut kernels. *Geophysical Journal International*, *160*(1), 195–216. https://doi.org/10.1111/j.1365-246X.2004.02453.x

Wang, S., Constable, S., Rychert, C., Harmon, N. (2020). A lithosphere-asthenosphere boundary and partial melt estimated using marine magnetotelluric data at the central Middle Atlantic Ridge. *Geochemistry, Geophysics, Geosystems*, *21*(9), e2020GC009177. https://doi.org/10.1029/2020GC009177

Wilson, D., Aster, R., & Team, T. R. (2003). Imaging crust and upper mantle seismic structure in the southwestern United States using teleseismic receiver functions. *The Leading Edge*, *22*(3), 232–237. https://doi.org/10.1190/1.1564528

Zhang, H., & Schmandt, B. (2019). Application of ps scattering kernels to imaging the mantle transition zone with receiver functions. *Journal of Geophysical Research*, *124*(1), 709–728. https://doi.org/10.1029/2018jb016274

Zhou, Y. (2018). Anomalous mantle transition zone beneath the Yellowstone hotspot track. *Nature Geoscience*, *11*(6), 449–453. https://doi.org/10.1038/s41561-018-0126-4